Geophysical Journal International

Geophys. J. Int. (2018) **212,** 872–890
Advance Access publication 2017 October 16
GJI Seismology

doi: 10.1093/gji/ggx447

Source parameters, path attenuation and site effects from strong-motion recordings of the Wenchuan aftershocks (2008–2013) using a non-parametric generalized inversion technique

Hongwei Wang, Yefei Ren and Ruizhi Wen

Key Laboratory of Earthquake Engineering and Engineering Vibration of China Earthquake Administration, Institute of Engineering Mechanics, China Earthquake Administration, No. 29 *Xuefu Road, Harbin* 150080*, China. E-mail: renyefei@iem.net.cn*

Accepted 2017 October 14. Received 2017 August 14; in original form 2016 October 11

SUMMARY

Secondary (*S*) wave amplitude spectra from 928 strong-motion recordings were collected to determine the source spectra, path attenuation and site responses using a non-parametric generalized inversion technique. The data sets were recorded at 43 permanent and temporary strong-motion stations in 132 earthquakes of M_s 3.2–6.5 from 2008 May 12 to 2013 December 31 occurring on or near the fault plane of the 2008 Wenchuan earthquake. Some source parameters were determined using the grid-searching method based on the omega-square model. The seismic moment and corner frequency vary from 2.0×10^{14} to 1.7×10^{18} N $\cdot$ m and from 0.1 to 3.1 Hz, respectively. The *S*-wave energy-to-moment ratio is approximately 1.32×10^{-5}. It shows that the moment magnitude is systematically lower than the surface wave magnitude or local magnitude measured by the China Earthquake Network Center. The seismic moment is approximately inversely proportional to the cube of the corner frequency. The stress drop values mainly range from 0.1 to 1.0 MPa, and are lognormal distributed with a logarithmic mean of 0.52 MPa, significantly lower than the average level over global earthquake catalogues. The stress drop does not show significant dependence on the earthquake size and hypocentre depth, which implies self-similarity for earthquakes in this study. The ε indicator was used to determine the stress drop mechanism. The low stress drop characteristic of the Wenchuan aftershocks may be interpreted by the partial stress drop mechanism, which may result from remaining locked sections on the fault plane of the main shock. Furthermore, we compared the stress drop distribution of aftershocks and slip distribution on the fault plane of the main shock. We found that aftershocks with higher stress drop occurred at areas with smaller slip in the main shock. The inverted path attenuation shows that the geometrical spreading around the seismogenic region of Wenchuan earthquake sequence is weak and significantly dependent on frequency for hypocentre distances ranging from 30 to 150 km. The frequency-dependent *S*-wave quality factor was regressed to $151.2f^{1.06}$ at frequencies ranging from 0.1 to 20 Hz. The inverted site responses provide reliable results for most stations. The site responses are obviously different at stations in a terrain array, higher at the hilltop and lower at the hillfoot, indicating that ground motion is significantly affected by local topography.

Key words: Fourier analysis; Earthquake ground motions; Earthquake source observation; Seismic attenuation; Site effects.

INTRODUCTION

The M_w 7.9 Wenchuan earthquake on 2008 May 12 was the strongest earthquake ever recorded along the Longmenshan fault belt. It was also one of the most destructive earthquakes in China, which caused catastrophic damage and heavy casualties and affected a wide range of regions. This event generated a surface rupture zone of 240 km in length along the Beichuan fault and an additional 72 km along the Pengguan fault (Xu *et al*. 2009).

Before the Wenchuan earthquake, the Longmenshan fault belt was not very active. In the past 100 yr, only two events of $M \geq 6.0$ have been recorded. One was the 1958 *M*6.2 Beichuan earthquake, which occurred on the Beichuan fault. The other was the 1970 *M*6.2 Dayi earthquake, which occurred on the Pengguan fault (Chen *et al*. 1994). However, lots of fragmentary ruptures frequently occurred on the Longmenshan fault belt, triggering a large number of small earthquakes with magnitudes ranging from 1.0 to 5.0 (Yang *et al.* 2005). Large ruptures occurred in recent years, including the 2008 M_w 7.9 Wenchuan earthquake and the 2013 M_w 6.6 Lushan earthquake, which implied that the Longmenshan fault belt was activated after a long silence. As a result, the design seismic accelerations for most areas in the Longmenshan region were substantially modified in the latest generation of seismic ground motion parameters zonation map of China, which was formally issued in 2015 (AQSIQ 2015). They were increased to 0.15 or 0.20*g* (*g*, gravitational acceleration) from 0.10 to 0.15*g*, respectively, in the previous version. Design seismic accelerations are divided into six levels in the zonation map of China, which gradually increase from 0.05 to 0.40*g* at an interval of 0.05 or 0.10*g*. The second, third and fourth levels are 0.10, 0.15 and 0.20*g*, respectively. This means that the seismic-proof demand was raised one level, or even two levels for most areas in the Longmenshan region, implying a current potential high seismic hazard in this region.

The attenuation laws for ground motions, scaling relations of source parameters and site effects are directly related to the prediction and assessment of seismic hazard. They play essential roles in establishing ground motion prediction equations or simulating ground motion time histories. Therefore, it is very valuable to study the source, path and site characteristics of earthquakes occurring on the Longmenshan fault belt such as the Wenchuan earthquake sequence. In recent years, such studies have already been performed, for example, Ren *et al.* (2013), Yu and Li (2012) and Hua *et al.* (2009). Ren *et al.* (2013) analysed the site responses of permanent strong-motion stations and identified the soil non-linearity using strong-motion recordings from the Wenchuan aftershocks, based on the parametric generalized inversion technique (GIT). However, path and source characteristics were not considered. The source parameters and quality factor of the propagation medium were inverted by Yu and Li (2012) using the Levenberg–Marquardt algorithm. However, only 13 aftershocks of $M > 5.0$ were investigated, and few analyses regarding site effects were made in this study. More than 1000 aftershocks of $M_L \geq 3.0$ were investigated by Hua *et al.* (2009) to study the segmentation features of the stress drop. However, other source parameters were not included, and site effects were neglected. There is not yet a study including systematic analyses on the source parameters, path attenuation and site effects of ground motions from the Wenchuan earthquake sequence.

In this paper, a non-parametric generalized inversion of secondary (*S*) wave amplitude spectra of the strong-motion recordings from the Wenchuan earthquake sequence was performed to separate the source, propagation path and site effects simultaneously. Earthquakes considered in this study occurred on or near the fault plane of the Wenchuan earthquake from 2008 May 12 to 2013 December 31. We investigated the attenuation characteristics, mainly including geometrical spreading and anelastic attenuation. Some source parameters were estimated from the inverted source spectra and then used to study the source scaling relations of earthquakes in this region. Finally, we provided the site responses for stations considered in this study, and analysed preliminarily the local topographic effect on ground motions.

DATA SET

A total of seven issues (Issues 12–18) of uncorrected strong-motion acceleration recordings have been officially issued in China by the China Strong Motion Network Center since the China National Strong Motion Observation Network System (NSMONS) formally began operation in 2007. The analogue recordings in China before 2007 were published in Issues 1–11. Issue 12 covers recordings from the Wenchuan main shock. Issues 13 and 14 cover recordings from the Wenchuan aftershocks obtained by the permanent and temporary stations, respectively. Issues 15, 16 and 18 cover other recordings collected during 2007–2009, 2010–2011 and 2012–2013, respectively. Issue 17 covers recordings from the 2013 Lushan earthquake sequence. Strong-motion recordings in Issues 13–16 and 18 from earthquakes that occurred on or near the rupture fault of the Wenchuan earthquake are used as the data set in this study. It is composed of more than 2000 strong-motion recordings from 383 M_s (M_L) 3.3–6.5 earthquakes from 2008 May 12 to September 30 recorded at 76 permanent stations of NSMONS in Gansu and Sichuan provinces (Issue 13), 2214 strong-motion recordings from 600 M_s (M_L) 2.3–6.3 earthquakes from 2008 May 14 to October 10 recorded at 83 temporary stations (Issue 14, Wen *et al.* 2014), and 355 additional strong-motion recordings from 57 M_s (M_L) 3.1–5.5 earthquakes from 2008 October 1 to 2013 December 31 recorded at 86 stations of NSMONS (Issues 15, 16 and 18). Deviations between the surface wave magnitude M_s and the local magnitude M_L for earthquakes in China and adjacent regions measured by the China Earthquake Network Center (CENC) were ignored (Zhang *et al.* 2008). In this paper, M_s was used to represent the measured magnitude by CENC. The baseline correction and a Butterworth bandpass filter between 0.1 and 30.0 Hz were performed.

Fig. 1 shows the hypocentre distance (*R*) and geometric mean of the peak ground acceleration (PGA) for the two horizontal components (east–west and north–south) of the strong-motion recordings in this data set. PGAs of these strong-motion recordings mainly vary from 2.0 to 100 cm s^{-2}. Hypocentre distances of most recordings from Issues 13, 15, 16 and 18 generally range from 30 to 200 km. However, hypocentre distances for many recordings from Issue 14 are less than 30 km, with the minimum approaching 1.0 km. Recordings from Issue 14 were obtained by temporary stations deployed as close to the seismogenic fault as possible (Wen *et al.* 2014). Very few recordings from Issues 15, 16 and 18 were obtained from earthquakes of $M_s > 5.0$ because very few aftershocks with large magnitudes occurred in the seismogenic area of the Wenchuan earthquake during 2009–2013. We selected available recordings from this data set according to the following criteria proposed by Ren *et al.* (2013): (1) 30 km $\leq R \leq$ 150 km; (2) 2 cm $s^{-2} \leq$ PGA $\leq$ 100 cm s^{-2}; (3) each selected earthquake should be recorded by at least four stations, each of which should collect at least four recordings that match (1) and (2). Finally, we employed 928 strong-motion recordings from 132 earthquakes of M_s 3.2–6.5 at 43 strong-motion stations. Earthquake epicentres and strong-motion stations considered in this study are shown in Fig. 2. Most stations are located in the mountains, west of

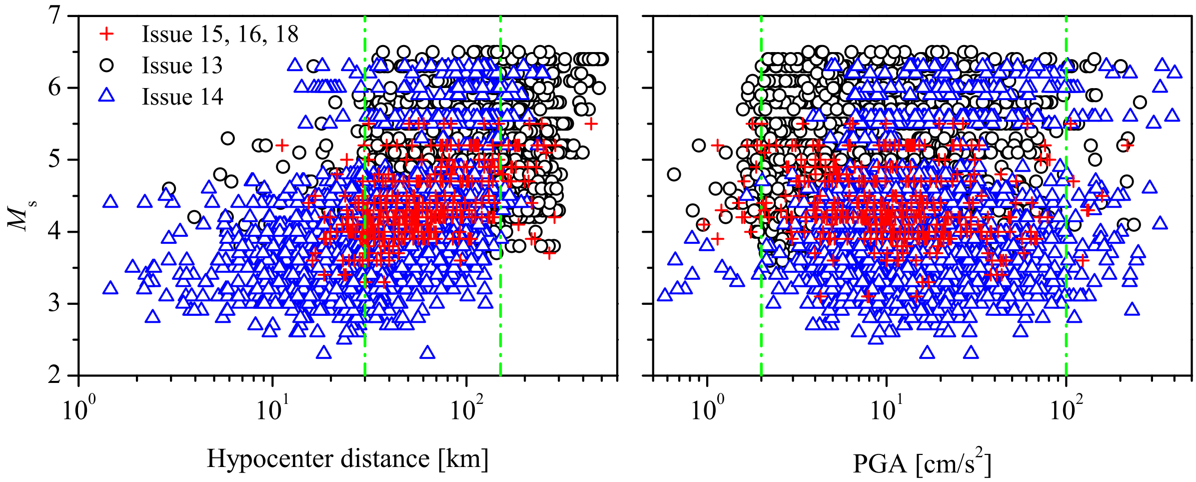

Figure 1. Hypocentre distance and peak ground acceleration (PGA) of the data set used in this study. The dashed–dotted lines in the left-hand panel represent the hypocentre distance range for most data in the Issues 13, 15, 16 and 18 released by China Strong Motion Network Center. The dashed–dotted lines in the right-hand panel represent the PGA range for most recordings of the data set used in this study. Issues 13 and 14 cover recordings from the Wenchuan aftershocks obtained by the permanent and temporary stations, respectively. Issues 15, 16 and 18 cover other recordings collected during 2007–2009, 2010–2011 and 2012–2013, respectively.

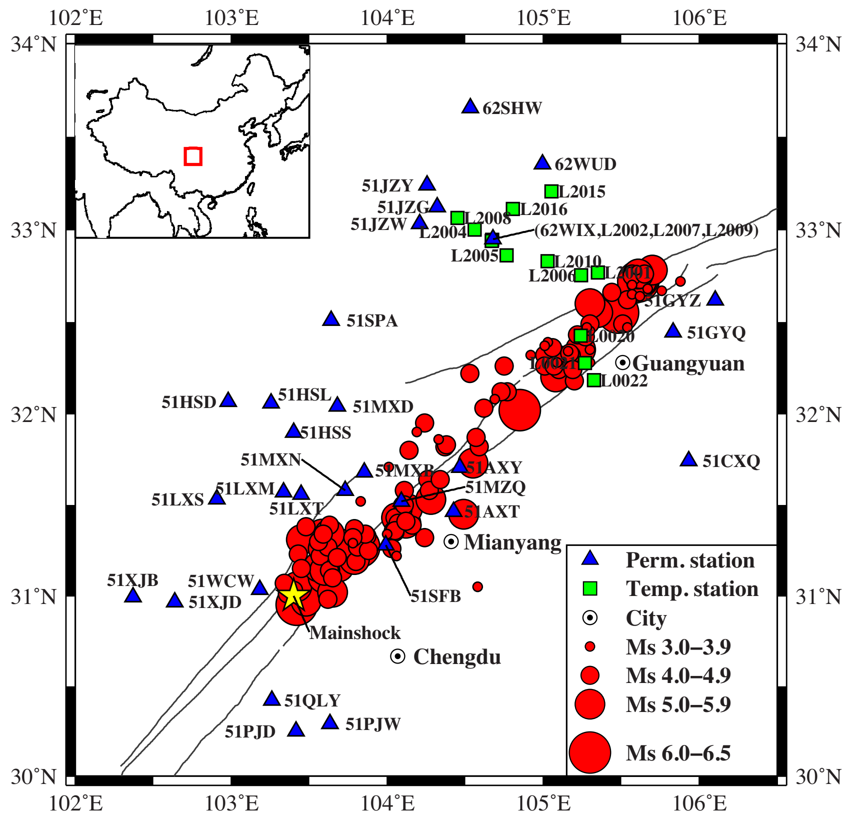

Figure 2. The locations of earthquakes (circle) and strong-motion stations (triangle and square) used in this study. The grey solid lines represent the surface traces of the Longmenshan fault belt. Insert in the top left corner shows the location of the study region in China.

the Longmenshan fault belt. In contrast to data used by Ren *et al*. (2013), we added more earthquakes and strong-motion stations in this study.

The *S* waves of the two horizontal components of the strong-motion recordings were extracted, according to studies of Husid (1967) and McCann (1979). A cosine taper was applied at the beginning and end of the *S*-wave window, and the length of each taper was set at 10 per cent of the total trace length (Hassani *et al*. 2011; Ren *et al*. 2013). The Fourier amplitude spectrum of the *S* wave was calculated and

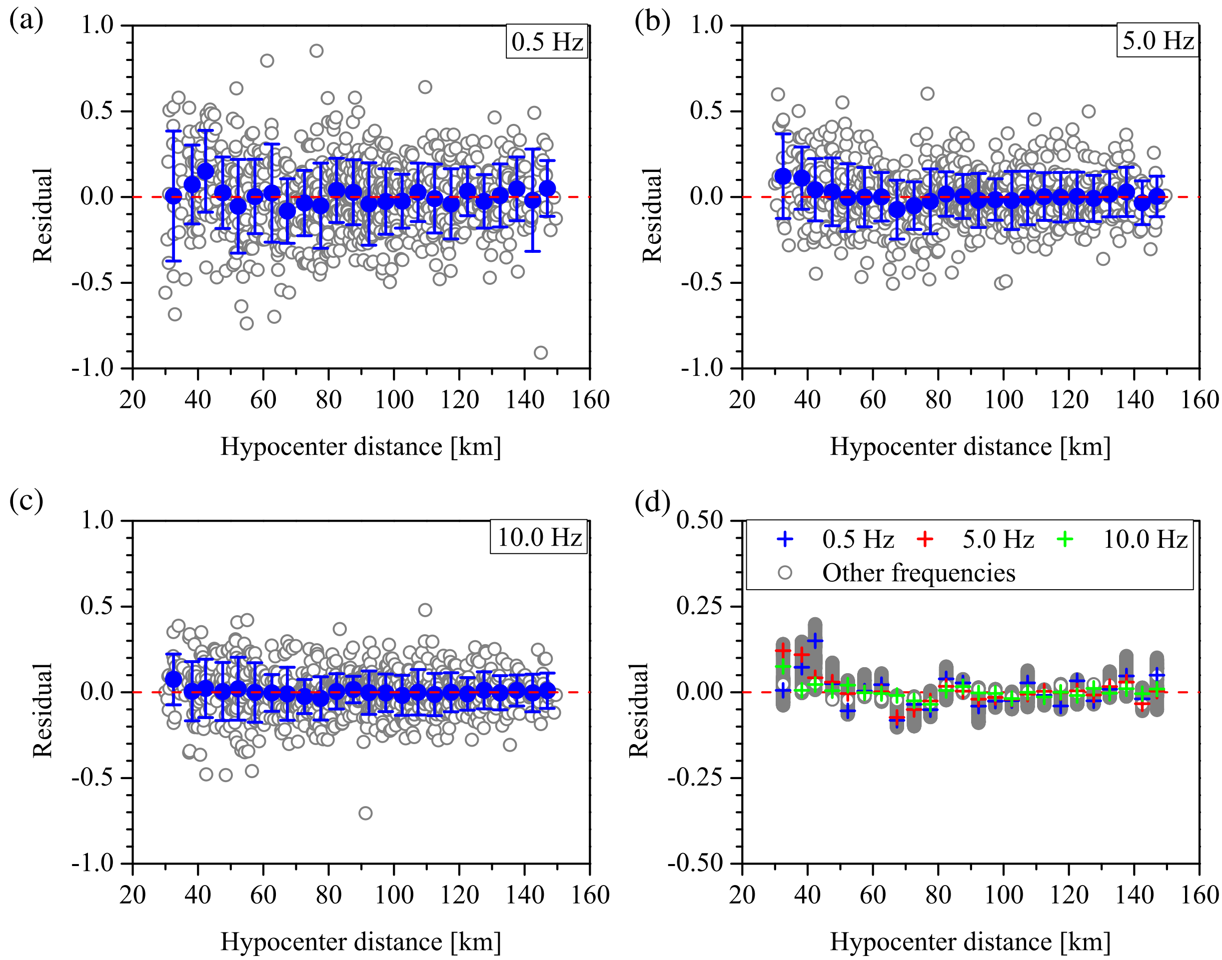

Figure 3. Residuals of synthetic results produced by the inverted source spectra, site responses and path attenuation, computed as log10 (observation/synthetics), versus hypocentre distance at (a) 0.5 Hz, (b) 5.0 Hz and (c) 10.0 Hz. The average residuals (blue circles) and one standard deviations (error bars) for different distance bins were computed. (d) The average residuals at each frequency of 0.1–20 Hz for different distance bins.

smoothed using the windowing function of Konno & Ohmachi (1998) with $b = 20$. The vector synthesis of the Fourier amplitude spectra from two horizontal components was used to represent the horizontal ground motion in frequency domain.

METHODOLOGY

We applied a two-step non-parametric GIT (Castro *et al.* 1990; Oth *et al.* 2008, 2009) to separate attenuation characteristics, source spectra and site response functions. In the first step, the dependence of the spectral amplitudes on the distance at frequency (f) can be expressed as:

$$O_{ij}\left(f, R_{ij}\right) = M_i\left(f\right) \cdot A\left(f, R_{ij}\right) \tag{1}$$

where $O_{ij}(f,R_{ij})$ is the spectral amplitude observed at the jth station resulting from the ith earthquake, R_{ij} is the hypocentre distance, $M_i(f)$ is a scale dependent on the size of the ith earthquake and $A(f, R_{ij})$ is a non-parametric function of distance and frequency accounting for the seismic attenuation (e.g. geometrical spreading, anelastic and scattering attenuation, refracted arrivals, etc.) along the path from source to site. $A(f, R_{ij})$ is not supposed to have any parametric functional form and is constrained to be a smooth function of distance with a value of 1 at reference distance R_0.

Once $A(f, R_{ij})$ is determined, the spectral amplitudes can be corrected for the seismic attenuation effect. In the second step, the corrected spectra are divided into source spectra and site response functions:

$$O_{ij}\left(f, R_{ij}\right) / A\left(f, R_{ij}\right) = S_i\left(f\right) \cdot G_j\left(f\right) \tag{2}$$

where $G_j(f)$ is the site response function at the jth station and $S_i(f)$ is the source spectrum of the ith earthquake. The trade-off between the site and source is resolved by selecting station 62WIX as a reference site, where the site responses are constrained to be 2.0 around all frequencies (Ren *et al.* 2013).

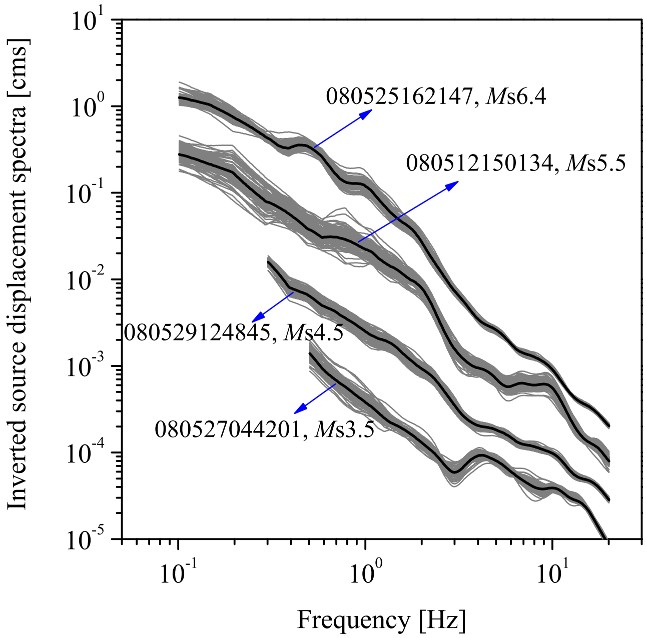

Figure 4. The inverted source spectra for four typical earthquakes representing four magnitude levels. The dark lines represent the inverted source spectra using the total recordings in this study. The grey lines represent the inverted source spectra from 100 bootstrap inversions. The name of the earthquake is composed of the date and time of this event.

Eq. (1) can be turned into a linear problem by taking the natural logarithm and expressing it as a matrix formulation:

$$\begin{bmatrix} 1 & 0 & 0 & 0 & \cdots & 0 & 1 & 0 & \cdots & 0 \\ 0 & 1 & 0 & 0 & \cdots & 0 & 0 & 1 & \cdots & 0 \\ \vdots & \vdots & \vdots & \vdots & \vdots & \vdots & \vdots & \vdots & \vdots & \vdots \\ 0 & 0 & 0 & 0 & \cdots & 1 & 0 & 0 & \cdots & 1 \\ \omega_1 & 0 & 0 & 0 & \cdots & 0 & 0 & 0 & \cdots & 0 \\ -\omega_2/2 & \omega_2 & -\omega_2/2 & 0 & \cdots & 0 & 0 & 0 & \cdots & 0 \\ 0 & -\omega_2/2 & \omega_2 & -\omega_2/2 & \cdots & 0 & 0 & 0 & \cdots & 0 \\ \vdots & \vdots & \vdots & \vdots & \vdots & \vdots & \vdots & \vdots & \vdots & \vdots \end{bmatrix} \cdot \begin{bmatrix} \ln A\,(f,\,R_1) \\ \ln A\,(f,\,R_2) \\ \ln A\,(f,\,R_3) \\ \ln A\,(f,\,R_4) \\ \vdots \\ \ln A\,(f,\,R_N) \\ \ln M_1\,(f) \\ \ln M_2\,(f) \\ \vdots \\ \ln M_1\,(f) \end{bmatrix} = \begin{bmatrix} \ln O_1\,(f,\,R_1) \\ \ln O_2\,(f,\,R_2) \\ \vdots \\ \ln O_N\,(f,\,R_N) \\ 0 \\ 0 \\ 0 \\ \vdots \end{bmatrix} \qquad (3)$$

In eq. (3), the hypocentre distance ranges are divided into N bins with a 5 km width. R_1, R_2 ..., R_N is a monotonically increasing sequence of hypocentre distance. The weighting factor ω_1 is used to constrain $A(f, R_0) = 1$ at reference distance R_0 and ω_2 is the factor determining the degree of smoothness of the solution. The reference distance was set to 30 km, which is the smallest hypocentre distance considered in this study.

We calculated the residuals between the observed data and the synthetic results from the product of the inverted source spectra, site responses and path attenuation, as shown in Fig. 3. The residuals were expressed as the logarithmic observed values minus logarithmic synthetic values. They vary around zero and have an average close to zero in the whole frequencies of 0.1–20 Hz. This shows that the residuals are independent on the hypocentre distance, indicating that the non-parametric inversion provides a good representation of the observed recordings considered in this study.

SOURCE SPECTRA

The bootstrap analysis proposed by Oth *et al.* (2008, 2011) was performed in this study to assess the stability of the inverted source spectra. 150 strong-motion recordings, accounting for approximately 16 per cent of the total recordings, were randomly removed from the data set, and the remaining ones were assembled as a new data set used in the inversion. We repeated this procedure 100 times to investigate the stability of the inverted source spectra. Fig. 4 shows the inverted source spectra resulting from 100 bootstrap inversions for four typical earthquakes representing four magnitude levels. The deviation from the source spectra obtained using the whole data set remains small, implying that the source spectra are stable.

Table 1. The basic information of a large earthquake and its four empirical Green's function (EGF) events used to estimate the cumulative attenuation within the reference distance of 30 km.

Large earthquakes							Small earthquakes as EGF events					
Number	Date and time	M_s/*M_w	Long. (°)	Lat. (°)	Depth (km)	M_w/f_c	Number	Date and time	M_s	Long. (°)	Lat. (°)	Depth (km)
01	08 08 05 174 916	6.5/6.0	105.61	32.72	13	5.86/0.206	02	08 06 19 182 559	4.4	105.62	32.73	10
						5.92/0.176	03	08 05 12 224 606	5.1	105.64	32.72	10
						6.12/0.109	04	08 05 27 160 322	5.3	105.65	32.76	15
						6.07/0.105	05	08 07 24 03 5443	5.7	105.63	32.72	10

*M_w is derived from the Global Centroid-Moment-Tensor (CMT) catalogue.

The cumulative attenuation within the reference distance is not included in the $A(f,R)$ derived from the first-step inversion. The inverted source spectra from the second-step inversion absorb this cumulative attenuation when the trade-off between the site and source is solved using the known site response of the reference site. Therefore, the real source spectrum can be expressed as:

$$S(f) = S_{\text{inverted}}(f)/\psi(f) \tag{4}$$

where $\psi(f)$ represents the cumulative attenuation within the reference distance and $S_{\text{inverted}}(f)$ is the inverted source spectrum. If the real source spectrum of an earthquake is known, the cumulative attenuation can be derived from eq. (4).

Assuming that the source spectrum follows the omega-square source model (Brune 1970),

$$S(f) = (2\pi f)^2 \cdot \frac{R_{\theta\Phi} V}{4\pi \rho_s \beta_s^3} \cdot \frac{M_0}{1 + (f/f_c)^2} \tag{5}$$

where $R_{\theta\Phi}$ is the average radiation pattern over a suitable range of azimuths and take-off angles set to 0.55. $V = 1/\sqrt{2}$ accounts for the portion of total S-wave energy in the horizontal components. ρ_s and β_s are the density and S-wave velocity in the vicinity of the source set to 2700 kg m^{-3} and 3.6 km s^{-1}, respectively. M_0 and f_c are the seismic moment and corner frequency. We used the relationship proposed by Hanks & Kanamori (1979) to convert moment magnitude (M_w) to M_0 (unit: dynecm $= 10^{-7}$ N · m):

$$\log M_0 = 1.5 \times (M_w + 10.7) \tag{6}$$

If a small earthquake is regarded as the empirical Green's function (EGF) event of a large earthquake, the differences of the path attenuation in the strong-motion recordings at the same station from large and small earthquakes can be neglected. Fourier amplitude spectral ratio $O_L(f)/O_S(f)$ can be approximately expressed as the theoretical source spectral ratio $S_L(f)/S_S(f)$,

$$\frac{O_L(f)}{O_S(f)} \approx \frac{S_L(f)}{S_S(f)} = \frac{M_{0L}}{M_{0S}} \cdot \frac{1 + (f/f_{cS})^2}{1 + (f/f_{cL})^2} \tag{7}$$

where subscripts L and S represent the large and small earthquakes, respectively. According to eq. (7), the values of seismic moment and corner frequency for both large and small earthquakes could be achieved by minimizing the differences between the Fourier amplitude spectral ratio of the observed strong-motion recordings averaged over all stations triggered in both earthquakes and the theoretical source spectral ratio.

In this study, an M_s 6.5 earthquake (No. 01) that occurred on 2008 August 5 at 17:49:16 (Beijing time) at the northeastern part of the Longmenshan fault was selected as a large event, and four other earthquakes (M_s 4.4, 5.1, 5.3 and 5.7) were selected as its EGF events. The basic information for these earthquakes is listed in Table 1, and their epicentres and the recorded strong-motion stations are shown in Fig. 5.

The grid-searching method was adopted to determine the best-fit seismic moment and corner frequency in eq. (7). The best-fitting theoretical source spectral ratios between large and small earthquakes are in good agreement with the Fourier amplitude spectral ratios calculated using observed strong-motion recordings at frequencies of 0.1–20 Hz, as shown in Fig. 6. The obtained M_w values range from 5.86 to 6.12 and the f_c values range from 0.105 to 0.206 Hz for the M_s 6.5 earthquake, as shown in Table 1. The values of M_w are in good agreement with the one from the Global Centroid-Moment-Tensor (CMT) catalogue, that is, 6.0. According to eq. (5), the theoretical source spectra of the M_s 6.5 earthquake were obtained, then the values of $\psi(f)$ were calculated using eq. (4), as shown in Fig. 6. It shows that the $\psi(f)$ is not strongly dependent on the selected EGF event, implying its stable estimation. In this study, we adopted the $\psi(f)$ derived from the spectral ratio between the M_s 6.5 and the M_s 5.3 earthquakes (i.e. Nos. 01 and 04 in Table 1), which is approximately median of all four $\psi(f)$. The source displacement spectra corrected using $\psi(f)$ are shown in Fig. 7 for seven magnitude bins from 3.0 to 6.5 at an interval of 0.5 mag. Source spectra at high frequencies are close to the ω^{-2} decay.

Note that for a proper quantification of the stability of $\psi(f)$, it would be useful to consider additional pairs of collocated large events/EGFs, in particular in the southwestern part of the fault. Unfortunately, such pairs are not available. Because the hypocentres of large and small earthquakes are not close enough to remove the difference of path attenuation from their sources to sites, or the strong-motion recordings obtained in both earthquakes are not enough to calculate the reliable spectral ratio between them.

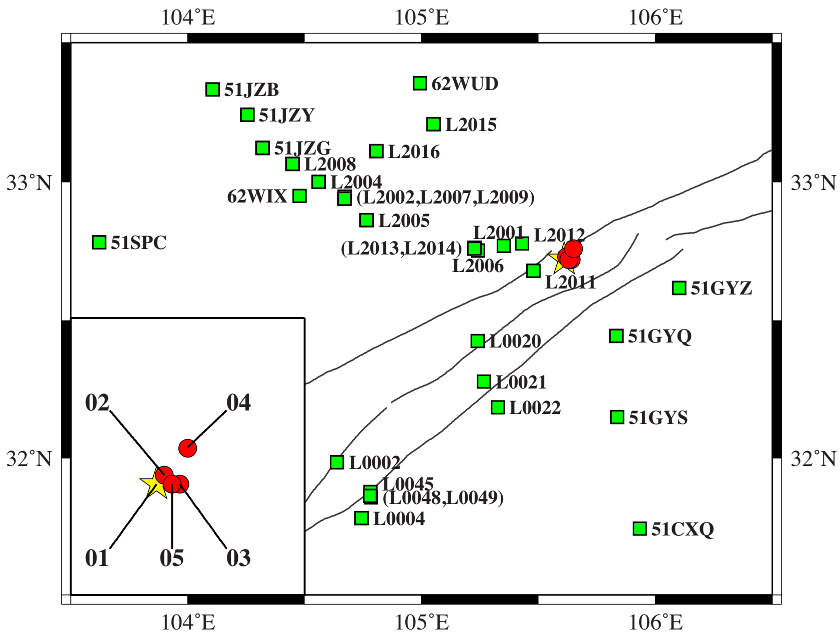

Figure 5. The epicentre locations of a large and four small earthquakes listed in Table 1, and strong-motion stations operating during these earthquakes.

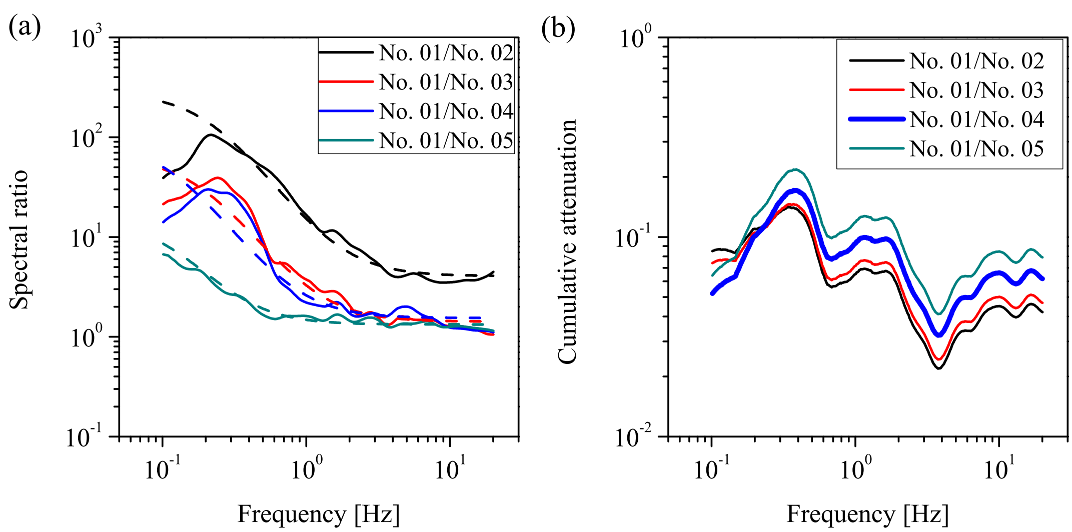

Figure 6. (a) The averaged Fourier amplitude spectral ratio (solid line) of strong-motion recordings observed at the same stations between the large and small earthquakes listed in Table 1, and the best-fit theoretical source spectral ratio (dashed line). (b) The cumulative attenuation within the reference distance of 30 km.

SOURCE PARAMETERS

The grid-searching method was adopted to obtain the best-fit seismic moment and corner frequency for each earthquake, making the theoretical source spectrum expressed by eq. (5) closest to the attenuation-corrected source spectrum. It can be represented as:

$$\sum_{m=1}^{Nf}\left\{\log_{10}\left[\frac{S_{i,\mathrm{inverted}}(f_m)/\Psi(f_m)}{S_i(f_m)}\right]\right\}^2 = \min. \quad (8)$$

$M_s - 1.0 \le M_w \le M_s + 1.0$, the corresponding searching ranges of M_0 are derived from eq. (6). The values of stress drop ($\Delta\sigma$) for small-to-moderate earthquakes generally vary from 0.1 to 100.0 MPa (Kanamori 1994). Following Brune (1970), the corner frequency is expressed as $f_c = 4.9 \times 10^6 \beta_s(\Delta\sigma/M_0)^{1/3}$. The searching ranges of f_c are estimated according to the possible variation ranges of $\Delta\sigma$. Fig. 7

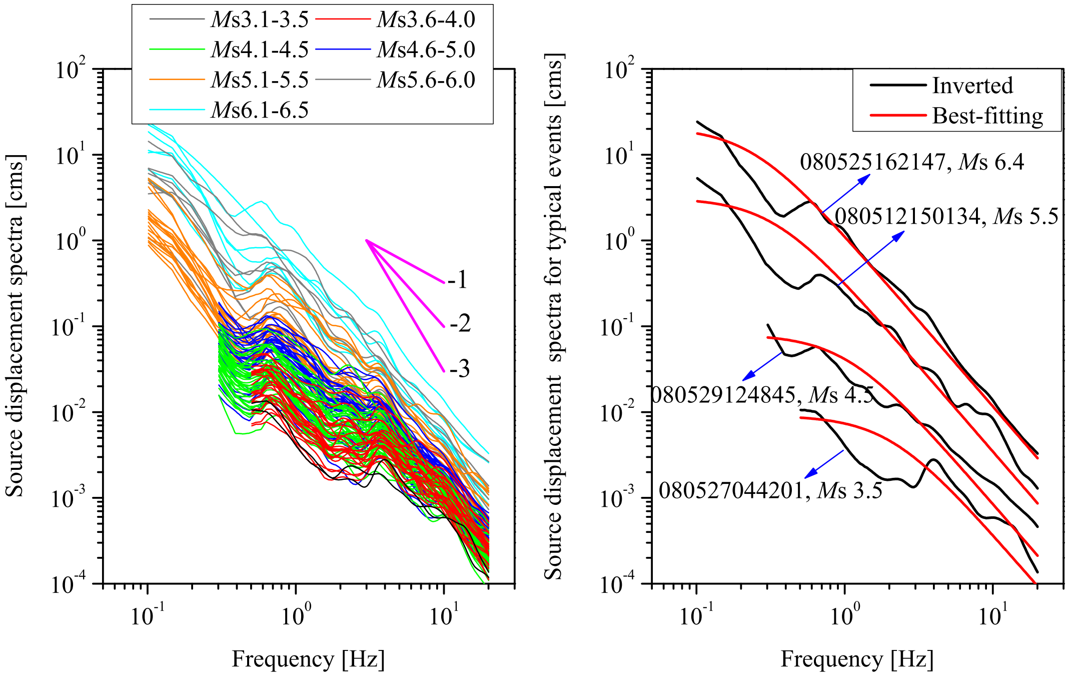

Figure 7. The attenuation-corrected source displacement spectra (left-hand panel), and the best-fitting theoretical source spectra to the inverted source spectra for four typical earthquakes representing four magnitude levels (right-hand panel).

shows some examples of the best-fitting theoretical source spectra. Then, the seismic moment and corner frequency were used to determine the stress drop and the source radius r according to the Brune (1970) source model:

$$r = \frac{2.34\beta_s}{2\pi f_c} \tag{9}$$

$$\Delta\sigma = \frac{7M_0}{16r^3} \times 10^{-13} \tag{10}$$

We also calculated the S-wave energy E_s in the frequency range from 0.01 to 30 Hz according to the relationship proposed by Vassiliou & Kanamori (1982):

$$E_s = \left[\frac{1}{15\pi\rho_s\alpha_s^5} + \frac{1}{10\pi\rho_s\beta_s^5}\right]\int_{-\infty}^{+\infty}\left[2\pi f\frac{M_0}{1+(1+f/f_c)^2}\right]^2 \mathrm{d}f \tag{11}$$

where $\alpha_s = 6.1$ km s^{-1} represents the primary (P) wave velocity. The apparent stress σ_a was calculated by the following relationship:

$$\sigma_a = \frac{\mu E_s}{M_0} \tag{12}$$

where $\mu = 3.5 \times 10^{10}$ N m^{-2} represents the rigidity modulus. All of these source parameters for earthquakes considered in this study are shown in Table 2.

Seismic moment M_0 and corner frequency f_c

The M_w values determined in this study are in good agreement with those derived from the Global CMT catalogue, although they are slightly higher than measurements provided by Zheng *et al.* (2009), as shown in Fig. 8(a). We obtained the relationship between M_w and M_s measured by CENC by a least-squares regression analysis:

$$M_w = (0.817 \pm 0.024)\, M_s + (0.650 \pm 0.111) \tag{13}$$

There are linear deviations between M_w and M_s measured by CENC. M_w is systematically lower than M_s for $M_s = 3.5$–6.5. This overestimation of M_s is more severe in the case of larger earthquakes with the maximum close to 0.5. In fact, such phenomena have been commonly found in other studies, such as in the 2013 April 20 Lushan earthquake sequence (Lyu *et al.* 2013), large numbers of small-to-moderate earthquakes in mainland China (Zhao *et al.* 2011), some small earthquakes in the Tangshan area (Matsunami *et al.* 2003), and earthquakes with magnitude greater than 4.0 in the Sichuan–Yunnan region of China (Xu *et al.* 2010a). This deviation may result from the inaccurate calibration functions and the neglect of the base correction in the process of measuring magnitude by CENC (Zhao *et al.* 2011).

Table 2. List of source parameters including moment magnitude (M_w), seismic moment (M_0), corner frequency (f_c), source radius (r), stress drop ($\Delta\sigma$), S-wave energy (E_s) and apparent stress (σ_a) determined in this study.

Earthquake*	M_s†	M_w	f_c (Hz)	M_0 ($\times 10^{14}$ N·m)	r (m)	$\Delta\sigma$ (MPa)	E_s ($\times 10^{11}$ J)	σ_a (MPa)
08 051 214 4315	6.3	5.41	0.275	1462.177	4867.92	0.555	21.224	0.435
08 051 214 5417	5.8	5.68	0.114	3715.352	11 772.07	0.100	9.756	0.079
08 051 215 0134	5.5	5.37	0.333	1273.503	4029.34	0.852	28.319	0.667
08 051 215 1345	4.7	4.33	0.849	35.075	1579.38	0.390	0.349	0.298
08 051 215 3442	5.8	4.87	0.429	226.464	3122.31	0.325	1.917	0.254
08 051 215 4416	4.6	4.27	0.917	28.510	1461.39	0.400	0.290	0.305
08 051 215 4533	4.7	4.46	0.534	54.954	2510.81	0.152	0.216	0.118
08 051 215 5821	4.3	3.84	1.617	6.457	828.98	0.496	0.079	0.367
08 051 216 0258	4.7	4.05	1.204	13.335	1113.68	0.422	0.142	0.318
08 051 216 0806	4.3	4.17	1.218	20.184	1100.86	0.662	0.336	0.499
08 051 216 1057	5.5	4.86	0.403	218.776	3328.92	0.259	1.478	0.203
08 051 216 2140	5.5	4.99	0.462	342.768	2901.62	0.614	5.463	0.478
08 051 216 2612	5.1	4.97	0.388	319.890	3456.09	0.339	2.825	0.265
08 051 216 4030	4.2	3.92	1.544	8.511	868.36	0.569	0.120	0.422
08 051 216 5039	4.8	4.52	0.713	67.608	1880.37	0.445	0.772	0.343
08 051 217 0659	5.2	4.74	0.446	144.544	3005.29	0.233	0.875	0.182
08 051 217 3115	5.2	4.88	0.386	234.423	3472.56	0.245	1.496	0.191
08 051 217 4224	5.3	5.10	0.382	501.187	3509.10	0.507	6.626	0.397
08 051 217 4457	4.2	3.85	2.386	6.683	561.80	1.649	0.262	1.178
08 051 217 4746	4.4	4.01	1.899	11.614	706.04	1.444	0.408	1.055
08 051 218 1915	4.0	3.53	2.904	2.213	461.74	0.984	0.051	0.686
08 051 218 2339	5.0	4.44	0.865	51.286	1550.34	0.602	0.788	0.461
08 051 218 4312	4.6	4.10	0.852	15.849	1573.14	0.178	0.072	0.136
08 051 218 5922	4.1	3.88	1.615	7.413	830.33	0.567	0.104	0.419
08 051 219 1101	6.3	5.82	0.137	6025.596	9790.57	0.281	44.566	0.222
08 051 219 3320	5.0	4.47	0.769	56.885	1744.21	0.469	0.684	0.360
08 051 220 1159	4.3	4.15	1.083	18.836	1237.99	0.434	0.207	0.329
08 051 220 1348	4.3	4.12	1.686	16.982	795.08	1.478	0.617	1.091
08 051 220 1540	4.9	4.60	0.645	89.125	2078.93	0.434	0.996	0.335
08 051 220 2958	4.6	4.21	0.869	23.174	1543.31	0.276	0.163	0.211
08 051 220 3855	4.2	3.83	1.768	6.237	758.20	0.626	0.096	0.460
08 051 221 4053	5.2	4.78	0.421	165.959	3184.61	0.225	0.970	0.175
08 051 222 1024	4.6	4.22	1.032	23.988	1299.60	0.478	0.290	0.363
08 051 222 1527	4.6	4.57	0.679	80.353	1975.16	0.456	0.943	0.352
08 051 222 4606	5.1	5.27	0.343	901.571	3913.37	0.658	15.486	0.515
08 051 223 0530	5.2	4.94	0.357	288.403	3755.63	0.238	1.792	0.186
08 051 223 0536	5.1	4.91	0.396	260.016	3382.50	0.294	1.990	0.230
08 051 223 1658	4.6	4.19	1.063	21.627	1261.10	0.472	0.258	0.358
08 051 223 2852	5.1	4.87	0.339	226.464	3950.27	0.161	0.950	0.126
08 051 223 5212	3.7	3.85	1.496	6.683	895.92	0.407	0.067	0.303
08 051 301 0311	4.6	4.45	0.959	53.088	1397.53	0.851	1.148	0.649
08 051 301 2906	4.9	4.42	0.996	47.863	1346.31	0.858	1.042	0.653
08 051 301 5432	5.1	5.06	0.313	436.516	4289.76	0.242	2.760	0.190
08 051 302 2617	4.1	3.91	1.164	8.222	1151.85	0.235	0.049	0.178
08 051 304 0849	5.8	5.39	0.309	1364.583	4338.34	0.731	26.077	0.573
08 051 304 4531	5.2	5.12	0.247	537.032	5427.58	0.147	2.068	0.116
08 051 304 4855	4.1	3.79	2.023	5.433	662.59	0.817	0.107	0.594
08 051 304 5127	4.7	4.56	0.844	77.625	1589.44	0.846	1.677	0.648
08 051 305 0813	4.5	4.08	1.399	14.791	958.60	0.735	0.271	0.549
08 051 307 4618	5.4	5.09	0.315	484.172	4260.99	0.274	3.464	0.215
08 051 307 5446	5.2	4.95	0.364	298.538	3683.91	0.261	2.034	0.204
08 051 308 2217	4.4	4.06	1.025	13.804	1307.56	0.270	0.094	0.205
08 051 309 0759	3.8	3.65	3.029	3.350	442.63	1.690	0.131	1.171
08 051 310 1516	4.3	4.05	1.484	13.335	903.53	0.791	0.262	0.589
08 051 310 3338	4.3	3.97	1.826	10.116	734.38	1.117	0.276	0.819
08 051 311 0954	4.0	3.50	3.051	1.995	439.41	1.029	0.047	0.712
08 051 314 3819	4.2	4.08	1.189	14.791	1127.96	0.451	0.168	0.340
08 051 314 3951	4.2	3.92	1.304	8.511	1028.18	0.343	0.073	0.257
08 051 315 0708	6.1	5.59	0.186	2722.701	7195.41	0.320	22.874	0.252
08 051 315 1916	5.1	4.87	0.449	226.464	2983.36	0.373	2.195	0.291
08 051 315 5303	4.7	4.51	0.998	65.313	1343.38	1.179	1.952	0.897
08 051 316 2052	4.8	4.56	0.824	77.625	1628.04	0.787	1.561	0.603
08 051 318 3642	4.3	4.18	1.370	20.893	978.29	0.976	0.509	0.731
08 051 323 3038	3.8	3.94	2.084	9.120	643.25	1.499	0.330	1.086
08 051 401 0126	3.7	3.61	1.895	2.917	707.68	0.360	0.026	0.263
08 051 409 0920	4.2	4.03	1.301	12.445	1030.37	0.498	0.155	0.374
08 051 409 5641	4.4	4.13	1.548	17.579	865.86	1.185	0.515	0.880

Table 2. (*Continued.*)

Earthquake*	M_s†	M_w	f_c (Hz)	M_0 ($\times 10^{14}$ N·m)	r (m)	$\Delta\sigma$ (MPa)	E_s ($\times 10^{11}$ J)	σ_a (MPa)
08 051 410 5437	5.8	5.45	0.178	1678.804	7514.41	0.173	7.638	0.136
08 051 411 0748	4.3	3.99	1.587	10.839	844.78	0.787	0.211	0.583
08 051 413 5457	4.7	4.66	0.609	109.648	2203.14	0.449	1.269	0.347
08 051 415 3217	3.9	3.77	1.557	5.070	861.19	0.347	0.044	0.258
08 051 417 2643	5.1	5.01	0.396	367.282	3382.93	0.415	3.969	0.324
08 051 505 0106	4.8	4.65	0.613	105.925	2187.79	0.443	1.209	0.342
08 051 510 0523	3.8	3.92	1.084	8.511	1236.86	0.197	0.042	0.149
08 051 520 1024	4.2	4.17	1.168	20.184	1147.99	0.584	0.297	0.441
08 051 605 5547	4.5	4.26	1.574	27.542	851.73	1.950	1.328	1.446
08 051 611 3426	4.9	4.52	0.803	67.608	1669.62	0.636	1.099	0.488
08 051 613 2547	5.9	5.39	0.269	1364.583	4983.35	0.482	17.235	0.379
08 051 801 0824	6.1	5.88	0.170	7413.102	7864.85	0.667	129.940	0.526
08 051 912 0856	4.6	4.38	1.069	41.687	1254.49	0.924	0.974	0.701
08 052 001 5233	5.0	4.76	0.608	154.882	2203.43	0.633	2.531	0.490
08 052 123 2954	4.3	4.22	1.242	23.988	1079.80	0.834	0.502	0.627
08 052 400 3546	4.0	4.01	1.339	11.614	1001.34	0.506	0.147	0.379
08 052 401 5332	3.9	4.03	1.471	12.445	911.31	0.719	0.222	0.536
08 052 516 2147	6.4	5.92	0.236	8511.380	5671.41	2.041	455.520	1.606
08 052 704 4201	3.5	3.58	1.838	2.630	729.49	0.296	0.019	0.217
08 052 716 0322	5.3	5.25	0.347	841.395	3865.42	0.637	13.993	0.499
08 052 716 1206	3.7	3.72	2.188	4.266	612.85	0.811	0.083	0.585
08 052 716 3751	5.7	5.41	0.395	1462.177	3390.63	1.641	62.484	1.282
08 052 721 5934	4.7	4.83	0.333	197.242	4025.71	0.132	0.681	0.104
08 052 801 3510	4.7	4.69	0.816	121.619	1642.96	1.200	3.731	0.920
08 052 912 4845	4.5	4.31	1.031	32.734	1299.85	0.652	0.541	0.495
08 053 114 2242	4.3	4.09	1.540	15.311	870.38	1.016	0.385	0.754
08 060 311 0928	4.6	4.67	0.524	113.501	2557.02	0.297	0.873	0.231
08 060 501 2643	4.2	4.20	0.926	22.387	1448.04	0.323	0.184	0.246
08 060 512 4106	4.8	4.66	0.639	109.648	2099.63	0.518	1.464	0.401
08 060 714 2832	4.2	4.08	1.589	14.791	843.95	1.077	0.393	0.798
08 060 806 1428	4.7	4.59	0.629	86.099	2129.89	0.390	0.865	0.301
08 060 906 5536	3.2	3.74	1.103	4.571	1215.62	0.111	0.013	0.084
08 061 010 1504	3.6	3.68	2.249	3.715	596.16	0.767	0.068	0.552
08 061 100 2728	4.0	4.18	1.290	20.893	1038.94	0.815	0.426	0.612
08 061 713 5142	4.3	4.18	1.100	20.893	1218.32	0.505	0.267	0.383
08 061 721 4044	4.1	4.08	1.409	14.791	951.80	0.750	0.276	0.561
08 061 918 2559	4.4	4.32	1.095	33.884	1224.26	0.808	0.691	0.612
08 062 112 0303	3.9	4.06	1.105	13.804	1212.93	0.338	0.118	0.256
08 062 218 3734	4.2	4.06	1.385	13.804	967.78	0.666	0.229	0.498
08 062 305 3831	4.0	4.00	1.478	11.220	907.15	0.658	0.183	0.490
08 062 805 4210	4.5	4.32	1.045	33.884	1282.83	0.702	0.602	0.533
08 062 907 5519	4.2	4.05	1.164	13.335	1151.95	0.382	0.128	0.288
08 071 706 2053	3.6	4.03	0.761	12.445	1761.33	0.100	0.032	0.077
08 072 401 3018	3.9	3.77	1.607	5.070	834.39	0.382	0.048	0.283
08 072 403 5443	5.7	5.61	0.223	2917.427	6000.10	0.591	45.221	0.465
08 072 413 3009	4.9	4.81	0.410	184.077	3269.25	0.230	1.104	0.180
08 072 415 0928	6.0	5.83	0.186	6237.348	7214.77	0.727	119.080	0.573
08 080 116 3242	6.2	5.70	0.241	3981.072	5556.24	1.015	105.960	0.798
08 080 202 1217	5.0	4.66	0.719	109.648	1865.87	0.738	2.079	0.569
08 080 221 2546	4.0	4.13	1.098	17.579	1220.59	0.423	0.188	0.320
08 080 517 4916	6.5	6.12	0.109	16 982.437	12 342.09	0.395	176.920	0.313
08 080 611 4227	4.2	4.19	1.183	21.627	1133.19	0.650	0.354	0.491
08 080 612 4706	4.3	4.22	1.172	23.988	1144.31	0.700	0.423	0.529
08 080 716 1534	5.0	4.66	0.809	109.648	1658.18	1.052	2.951	0.807
08 080 920 1020	3.9	4.05	0.894	13.335	1499.91	0.173	0.059	0.132
08 081 305 0321	4.5	4.42	1.146	47.863	1170.07	1.307	1.577	0.988
08 081 316 4543	3.8	3.89	1.634	7.674	820.35	0.608	0.115	0.450
08 083 115 2451	3.6	3.83	2.188	6.237	612.68	1.187	0.178	0.855
110 323 080 308	3.9	3.74	2.113	4.571	634.54	0.783	0.086	0.566
110 506 184 815	4.1	3.70	1.973	3.981	679.53	0.555	0.054	0.404
110 507 082 112	3.9	3.71	2.340	4.121	572.89	0.959	0.094	0.686
110 605 132 145	4.2	4.00	1.258	11.220	1065.80	0.405	0.114	0.305
110 904 121 345	4.2	3.97	1.606	10.116	835.01	0.760	0.190	0.563
111 101 055 815	5.2	4.99	0.592	342.768	2264.50	1.291	11.428	1.000
111 226 004 652	4.7	4.44	0.875	51.286	1532.62	0.623	0.815	0.477

*The earthquake number is composed of the data and time of this earthquake, for example, 08 051 214 4315 represent a earthquake occurred on 2008 May 12 at 14:43:15 (Beijing time).

†We ignore the deviation between the surface wave magnitude M_s and the local magnitude M_L measured by CENC. M_s is used to uniformly represent the M_s and M_L.

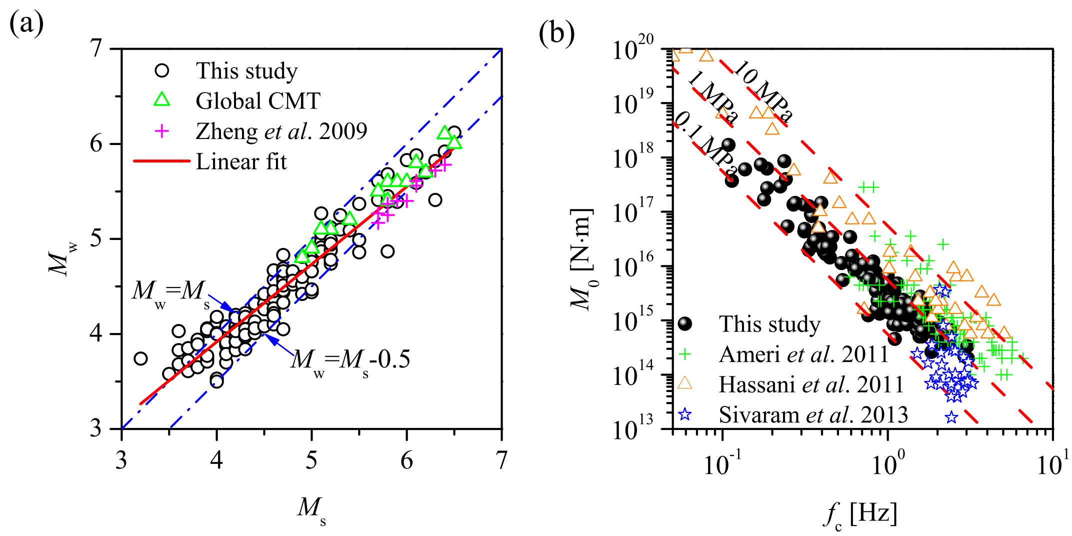

Figure 8. (a) Moment magnitude M_w derived from this study versus M_s measured by CENC. The solid line represents the best least-squares fit. The dashed–dotted lines represent the relationship of $M_w = M_s$, and $M_w = M_s - 0.5$. The triangles and crosses represent the M_w values determined by Global CMT and Zheng *et al*. (2009), respectively. (b) Seismic moment M_0 versus corner frequency f_c. The dashed lines represent the relationship between M_0 and f_c for various constant stress drops as indicated on the top of each line. The triangles, crosses and stars represent the relation of M_0 versus f_c derived from Ameri *et al*. (2011), Hassani *et al*. (2011) and Sivaram *et al*. (2013), respectively.

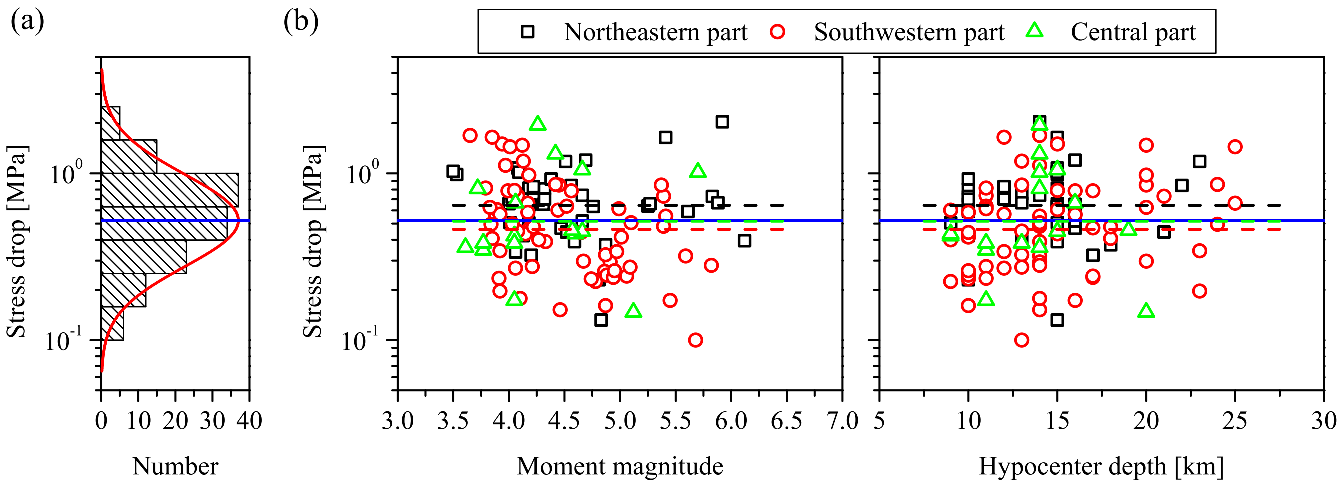

Figure 9. (a) The distribution of stress drops and the fitted lognormal distribution (red line). (b) The stress drop versus the moment magnitude (left) and the hypocentre depth (right). The dashed lines represent the logarithmic average of the stress drop of aftershocks that occurred at the northeastern, southwestern and central fault segments, respectively. The solid line represents the logarithmic average of the stress drop over all aftershocks.

Fig. 8(b) shows the plots of seismic moment versus corner frequency for the earthquakes considered in this study. These are also compared with the constant stress drop relations corresponding to 0.1, 1 and 10 MPa. The M_0 and f_c vary from 2.0×10^{14} to 1.7×10^{18} N · m and from 0.1 to 3.1 Hz, respectively. Corner frequencies in our study are significantly lower than those obtained in the 2009 L'Aquila earthquake sequence (Ameri *et al*. 2011) and earthquakes in central-eastern Iran (Hassani *et al*. 2011), which implies the lower stress drop. Some much smaller earthquakes in Kumaon Himalaya, India also provide a similar distribution of M_0 versus f_c with a low stress drop (Sivaram *et al*. 2013). The seismic moment is approximately inversely proportional to the cube of the corner frequency in this study, that is, $M_0 \propto f_c^{-3}$, and the data regression yields:

$$\log M_0 = (15.459 \pm 0.278) - 3.0 \log f_c \tag{14}$$

$M_0 f_c^3$ is equal to 2.87×10^{15} N · m · s^{-3}, which corresponds to a constant stress drop of 0.522 MPa according to the Brune (1970) model.

Stress drop

The stress drop values mainly vary from 0.1 to 1.0 MPa (Fig. 9), which are consistent with the results (≤1.0 MPa) given by Hua *et al*. (2009) for most of the Wenchuan aftershocks. They do not exhibit a significant dependence on the moment magnitude and hypocentre depth (Fig. 9), which indicates that the earthquakes considered in this study follow self-similarity with a constant stress drop. Studies from Allmann &

Shearer (2009), Oth *et al*. (2010), Zhao *et al*. (2011), etc. all confirmed the self-similarity of global earthquakes. However, some other studies obtained conflicting results, in which the self-similarity is broken down in some specific earthquake sequences (e.g. Tusa *et al*. 2006; Drouet *et al*. 2010; Mandal & Dutta 2011; Pacor *et al*. 2016).

The stress drops are nearly lognormal distributed with a logarithmic mean of 0.52 MPa, which is dramatically lower than the median value of 3.31 MPa for interplate earthquakes (Allmann & Shearer 2009). The Wenchuan aftershocks have small stress drop values in comparison to other large earthquake sequences, such as the 2010–2011 Canterbury, New Zealand earthquake sequence with stress release of 1–20 MPa (Oth & Kaiser. 2014), the 1983 M_{JMA} 7.7 Japan sea earthquake sequence with stress release of 1–30 MPa (Iwate & Irikura 1988), etc. They are also much smaller than the value of the main shock, which is approximately 1–3 MPa for different finite fault-slip models (Bjerrum *et al*. 2010). However, the Wenchuan main shock has a stress drop value similar to other earthquakes of the same magnitude, for example, the 2001 M_{w} 7.8 Kunlun, China earthquake and the 2002 M_{w} 7.7 Denali, Alaska earthquake (Shaw 2013). Therefore, the Wenchuan aftershocks are characterized by obvious low values of stress drop. This characteristic was also observed in some other earthquakes, such as the 2010 JiaSian, Taiwan earthquake (Hwang 2012), and for several smaller earthquakes in the Garhwal Himalaya region (Sharma & Wason 1994).

Shaw *et al*. (2015) proposed a physical model that shows reduced stress drops for nearby aftershocks compared to similar magnitude main shocks, because they rerupture part of the fault ruptured by the main shock which may have been partially healed. This model was supported by ground motion observations, showing smaller ground motions generated by nearby aftershocks (e.g. Abrahamson *et al*. 2014). Smaller values of aftershock stress drops have been also observed using corner frequency analysis of seismic sequences (e.g. Drouet *et al*. 2011).

In this study, an indicator ε proposed by Zuniga (1993) was used to investigate the stress drop mechanism of the Wenchuan earthquake sequence:

$$\varepsilon = \frac{\Delta\sigma}{\sigma_a + \frac{\Delta\sigma}{2}} \tag{15}$$

$\varepsilon < 1.0$ implies a partial stress drop mechanism where the final stress is greater than the dynamic frictional stress (Brune 1970; Brune *et al*. 1986), whereas $\varepsilon > 1.0$ indicates that frictional overshoot has occurred with the final stress lower than the dynamic frictional stress (Savage & Wood 1971). The well-known Orowan's hypothesis is met when $\varepsilon = 1.0$ (Orowan 1960). In this study, ε equals 0.75–0.85, which indicates that the Wenchuan aftershocks can be interpreted by the partial stress drop mechanism. Sharma & Wason (1994) pointed out that such kind of aftershocks occur either when the fault locks (heals) itself soon after the rupture of the main shock passes, so the average dynamic frictional stress drops over the whole fault, or when the stress release is not uniform and not coherent over the whole fault plane, and behaves like a series of multiple events with parts of the fault remaining locked. The blank area of the seismic moment release in the ruptured area during the Wenchuan earthquake, as well as the absence of the larger aftershocks, indicates a possibility of fault lock at the unruptured areas on the fault plane (Chen *et al*. 2013). The low stress drop may be related to parts of the fault remaining locked on the fault plane. The apparent stress of $M \geq 3.0$ earthquakes during 2000–2004 in the Sichuan province calculated by Cheng *et al*. (2006) is approximately proportional to $0.21\Delta\sigma$. This means that ε equals 1.4 (eq. 15), indicating frictional overshoot prevails over partial stress drop. The stress drop mechanism associated with earthquakes along the Longmenshan fault belt changed after the Wenchuan earthquake.

The stress drop spatial distribution was obtained by assembling and interpolating the values of all 132 aftershocks, compared with the slip distribution on the fault plane of the main shock, which was determined by Fielding *et al*. (2013), as shown in Fig. 10. Aftershocks were mainly concentrated on the southwest and northeast segments of the Beichuan fault, and less on the central part. Stress drop contours were generated in three segments from southwest to northeast, respectively. The higher slips emerged on the southwestern segment close to Wenchuan County. In the main shock, the Pengguan Massif began to rupture, and a large amount of stress was released on this segment (Chen *et al*. 2009). As a result, smaller stress releases occurred for aftershocks here, with a logarithmic average of stress drop of 0.46 MPa. However, the logarithmic average of stress drop is higher, approximately 0.64 MPa for the northeastern segment near the Qingchuan County. This segment also consists of Precambrian quartzite or other stiff geological bodies. Slip on this segment is relatively smaller, and the released stress is lower. The logarithmic average of the stress drop on the central segment is close to 0.52 MPa, and the median slip value corresponds to the median stress drop. Therefore, we infer that the stress drop of the aftershocks may be related to the slip distribution on the fault plane of the main shock. Higher stress release for aftershocks occurred in areas with lower slip in the main shock.

For further verifying the above inference, we investigated the magnitude and hypocentre depth distribution between northeastern and southwestern segments, as shown in Fig. 9. The results show that both segments have a homogeneous distribution of magnitude ranging from 3.5 to 6.0, and a homogeneous distribution of depth ranging from 8 to 25 km. Furthermore, the stiffness of crustal structure shows few changes over the whole ruptured area of the Wenchuan main shock according to the CRUST1.0 model (Laske *et al*. 2013). Therefore, the magnitude, hypocentre depth and crust stiffness could be excluded from the cause of inhomogeneous distribution of stress drop between two segments.

Radiated energy and apparent stress

Fig. 11 shows the *S*-wave energy E_{s} versus M_0. The relation between E_{s} and M_0 was obtained assuming $E_{\mathrm{s}} \propto M_0$:

$$\log E_{\mathrm{s}} = (-4.88 \pm 0.27) + \log M_0 \tag{16}$$

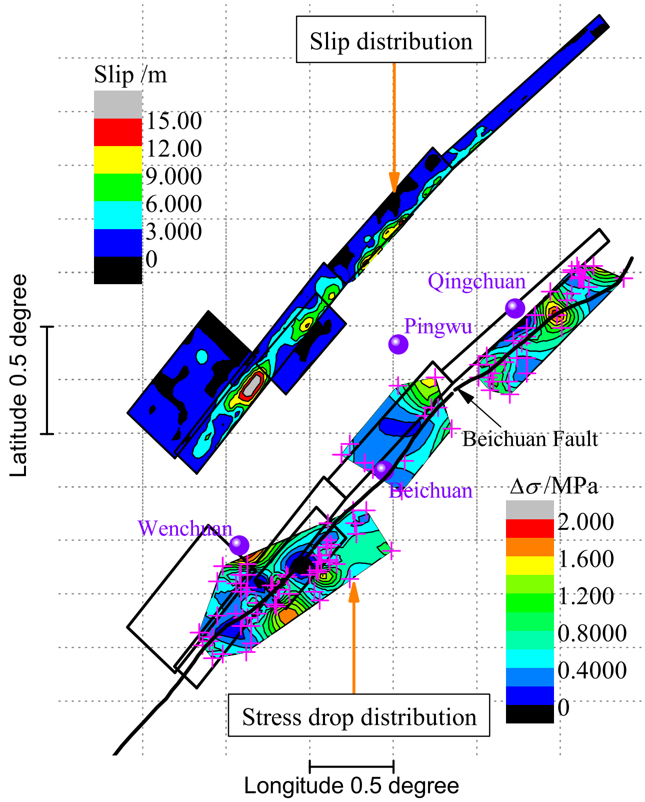

Figure 10. Slip distribution on the fault plane of the Wenchuan main shock determined by Fielding *et al*. (2013) and the stress drop contours for aftershocks employed in this study. The cross represents the epicentre of the aftershocks. In order to clearly compare the slip distribution and the stress drop of the aftershocks, the panel of the slip distribution is parallel moved upward.

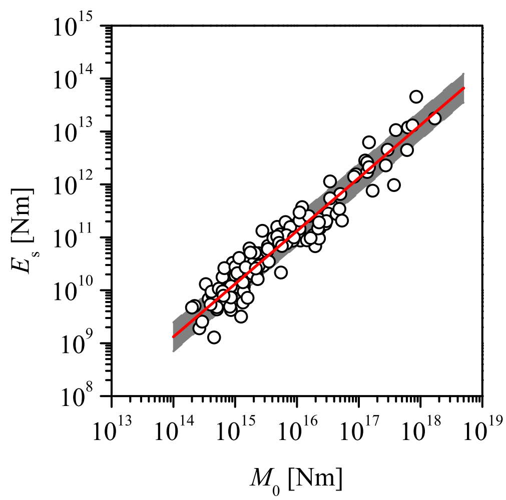

Figure 11. *S*-wave energy E_s versus seismic moment M_0. The regression line (solid) corresponding to constant apparent stress is shown within one standard deviation range (shaded area).

This relationship means that the *S*-wave energy-to-moment ratio is approximately equals to 1.32×10^{-5}, which is consistent with the result of 1.2×10^{-5} for small earthquakes in Anchorage, Alaska derived by Dutta *et al*. (2003). As shown in Table 2, the apparent stress σ_a varies from 0.077 to 1.606 MPa, which is directly proportional to $0.74\Delta\sigma$ with a correlation coefficient of 0.998. The apparent stress is independent of the earthquake size, since $\Delta\sigma$ is independent of M_0, as mentioned above.

ATTENUATION CHARACTERISTICS

The attenuation curve $A(f, R)$ can be described in terms of anelastic attenuation and other factors (Δ) related to seismic attenuation:

$$\ln A\,(f,\,R) - \ln\Delta = -\frac{\pi f}{Q_s\,(f)\,\beta_s}\,(R - R_0) \tag{17}$$

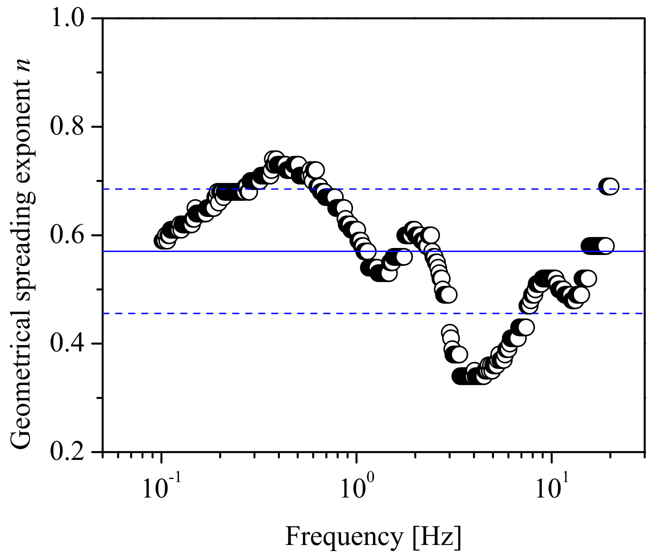

Figure 12. Geometrical spreading exponents (n) at frequencies ranging from 0.1 to 20 Hz. The solid and dashed lines represent the average n and one standard deviation range, respectively.

where Q_s stands for the S-wave quality factor dependent on the frequency. Δ must be greater than $A(f, R)$. Suppose Δ only contains the geometrical spreading in this study. In general, the geometrical spreading can be a linear, hinged bilinear, or hinged trilinear model of R. In this study, geometrical spreading is a simple model expressed as $(R_0/R)^n$, where n is the geometrical spreading exponent. The greater the n value is, the stronger the geometrical spreading. According to the necessary condition of $\ln A(f,R) - \ln(R_0/R)^n < 0$, we seek out a maximum n to meet this condition for each frequency, indicating the strongest geometrical spreading. Then Q_s can be evaluated from the slope of a linear least-squares fit of eq. (17) at each frequency.

In this study, both geometrical spreading and anelastic attenuation were considered frequency dependent in order to deal with the trade-off between them. This strategy was also used in the study of Bindi *et al*. (2004). The geometrical spreading exponents at frequencies of 0.5–20 Hz for $R = 30$–150 km are shown in Fig. 12. The values of n vary from 0.35 to 0.75, increasing with increased frequency from 0.1 to 0.4 Hz at first, then overall decreasing until a critical frequencyaround 3.5 Hz, and finally increasing up to 20 Hz, which indicates frequency-dependent geometrical spreading in this region. Frequency-dependent geometrical spreading was also observed in North America by Babaie Mahani & Atkinson (2013) through studying response spectral amplitudes and PGAs of ground motions. Geometrical spreading in the Northeast, central United States (CUS), and the Pacific Northwest/southwestern British Columbia (PNW/BC) has a tendency to decrease at first and then increase with the increased frequency, which is very similar to what we observed in this study.

Based on the analyses of larger numbers of strong-motions recordings, previous studies have shown that n is not lower than 1.0 for local distances, while n is approximately equal to 0.5 for regional distances (Atkinson & Mereu 1992; Bora *et al*. 2015). The threshold for local and regional distance is related to the crustal thickness. Our study region is located at the southeast margin of the Tibetan Plateau where the crustal thickness is about 50 km. Therefore, we regard 75 km (i.e. 1.5 times of crustal thickness) as the boundary between the local and regional distances (Atkinson & Mereu 1992). A general geometrical spreading model $(R_0/R)^{1.0}$ for $R < 75$ km, and $(R_0/75)(75/R)^{0.5}$ for $R \geq 75$ km is assumed. In this study, n is lower than 0.5 at frequencies ranging from 3 to 15 Hz, and 0.5–0.75 at frequencies lower than 3 Hz and greater than 15 Hz (Fig. 12). The average n value is 0.57 with a standard deviation of 0.11, obtained over frequencies ranging from 0.1 to 20 Hz. We compared the average geometrical spreading $(R_0/R)^{0.57}$ with the general geometrical spreading mentioned above, as shown in Fig. 13. We also compared the geometrical spreading in Yunnan and southern Sichuan determined by Xu *et al*. (2010b), which reflects a weak attenuation of ground motion. The average geometrical spreading in this study is slightly stronger than the one given by Xu *et al*. (2010b), while much weaker than the general geometrical spreading. This result implies that regions near the ruptured fault of the Wenchuan earthquake show weak geometrical spreading. Boore *et al*. (2014) determined that the observed ground motions from China, mainly derived from the Wenchuan earthquake sequence, exhibit a weaker attenuation, which is ascribed to a 'high Q'. This may also be related to the weak geometrical spreading inferred from our study. As shown in eq. (17), the path attenuation mainly consists of geometricalspreading and anelastic attenuation (represented by Q), a potential trade-off is inherent between them.

The S-wave quality factor Q_s versus frequency from 0.1 to 20 Hz is shown in Fig. 14. $Q_s(f)$ is regressed in the form of $Q_{s0}\, f^{\,\eta}$, and the least-squares solution is given by $151.2f^{1.06}$. Other studies also provided the Q_s values for the adjacent region (Fig. 14). Hua *et al*. (2009) obtained the Q_s for the western mountains ($274.6f^{0.423}$) and eastern plains ($206.7f^{0.836}$) in northern Sichuan, separated by the Longmenshan fault belt. Zhao *et al*. (2011) also determined $Q_s = 191.8f^{0.59}$ for western Sichuan. Compared with results from Hua *et al*. (2009) and Zhao *et al*. (2011), Q_{s0}, representing the quality factor at 1.0 Hz, is lower in our study. However, the attenuation coefficient η is much greater than that at the mountains but close to that at the plains. Q_s is closer to the results for the plains from Hua *et al*. (2009). The study region in this

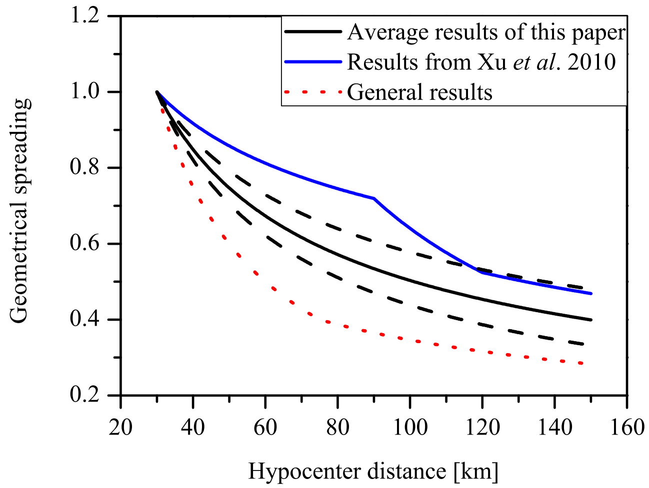

Figure 13. Comparison of the average geometrical spreading derived in this study with the general geometrical spreading, and results from Xu *et al*. (2010b). The averaged results of this study represent $(R_0/R)^{0.57}$ over the hypocentre distance from 30 to 150 km. Two dashed lines represent the plus or minus one standard deviation of the average. The general results represent $(R_0/R)^{1.0}$ for $R < 75$ km and $(R_0/75)(75/R)^{0.5}$ for $R \geq 75$ km.

paper is located on both sides of the Longmenshan fault belt, where the elevation suddenly drops from about 4500 m on the plateau to 500 m in the Sichuan Basin. The low Q_{s0} and high η may be related to the propagation path passing through the highly heterogeneous active fault belt.

SITE RESPONSE

The calculated site response functions of the 43 strong-motion stations are shown in Fig. 15. Site responses for most stations are generally in good agreement with those determined by Ren *et al*. (2013). Compared with the site responses derived from the horizontal-to-vertical spectral ratio (HVSR) method (Fig. 15), predominant frequencies are approximately identical, while site amplifications from the non-parametric GIT are significantly higher, except for some stations (51SFB, 51SPA, 51QLY and L0021). That is because the HVSR method can approximately evaluate the predominant site frequency but underestimates the site amplification (Castro *et al*. 2004; Hassani *et al*. 2011).

Since many analyses related to site effects in the Wenchuan earthquake sequence have been made in the study of Ren *et al*. (2013), our study only focused on the performance of a terrain effect array in the Wenchuan aftershocks. Stations L2009, L2002 and L2007 compose a terrain effect array, which were installed on the top (altitude 969 m), middle (altitude 960 m) and foot (altitude 927 m) of a hill (Wen *et al*. 2014). Fig. 16(a) shows the locations of the three stations on the hill, which share similar geological conditions. The site response functions of the three stations determined by the non-parametric GIT and HVSR method are shown in Fig. 16(b). Site responses from non-parametric GIT have significant discrepancies among the three stations, especially at frequencies of 2.0–8.0 Hz. Site amplification increases with the

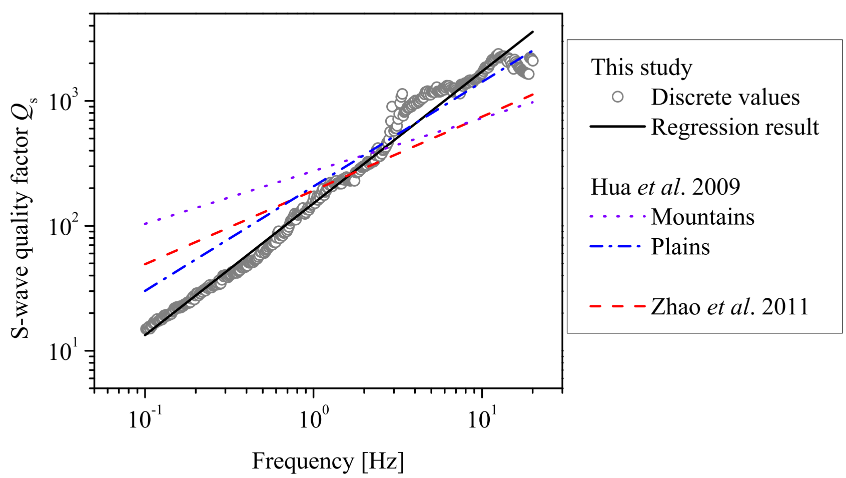

Figure 14. Frequency-dependent *S*-wave quality factor Q_s derived from this study. The solid line represents the least-squares regression of this study in the frequency range 0.1–20 Hz, that is, $Q_s(f) = 151.2f^{1.06}$. The dotted line and the dashed–dotted line represent $Q_s(f) = 274.6f^{0.423}$ for the western mountains and $Q_s(f) = 206.7f^{0.836}$ for the eastern plains in the northern Sichuan from the study of Hua *et al*. (2009). The dashed line represents $Q_s(f) = 191.8f^{0.56}$ for western Sichuan from Zhao *et al*. (2011).

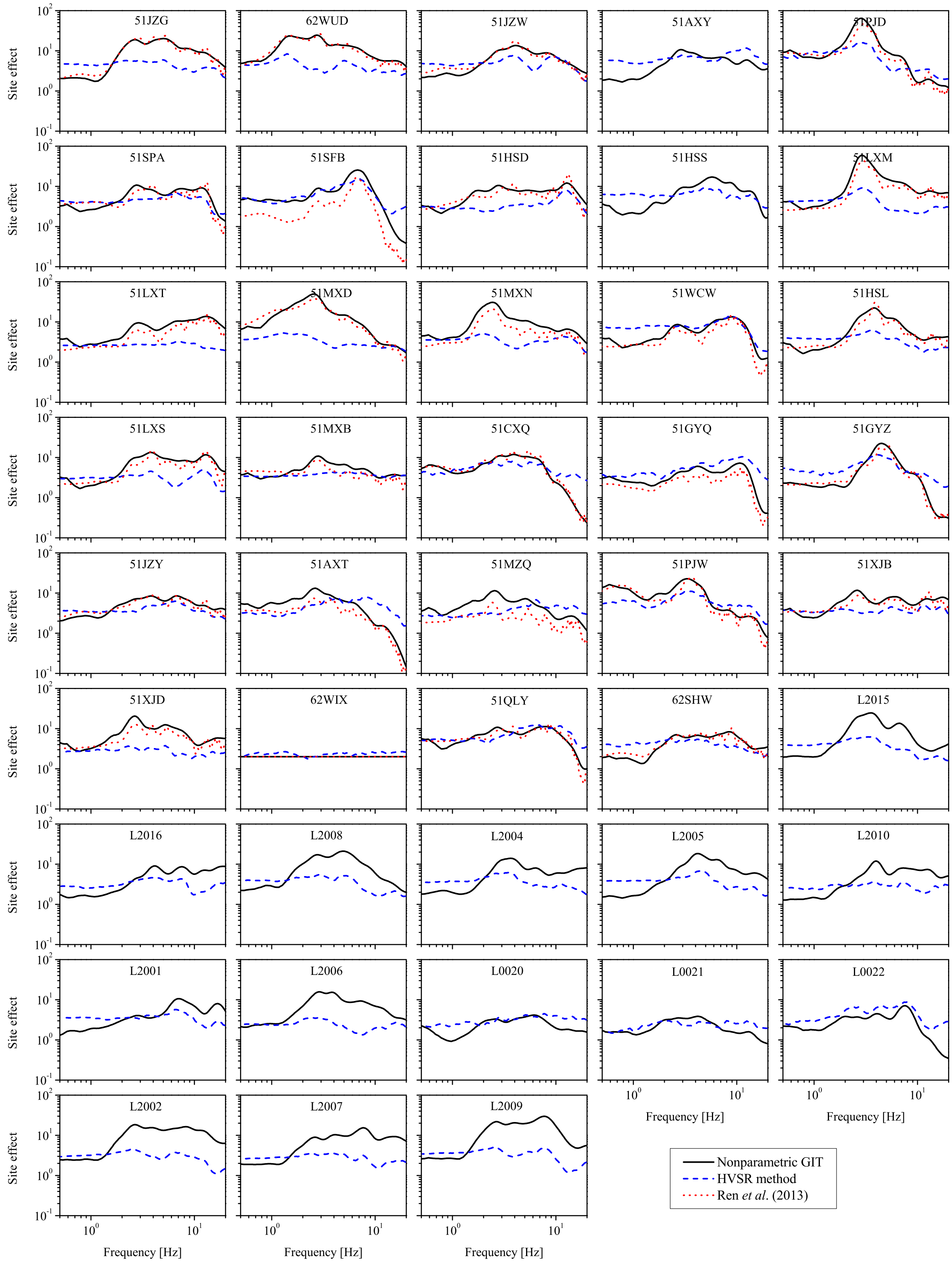

Figure 15. Site response functions derived from the non-parametric GIT, HVSR method and Ren *et al*. (2013). The locations of these stations are clearly shown in Fig. 2.

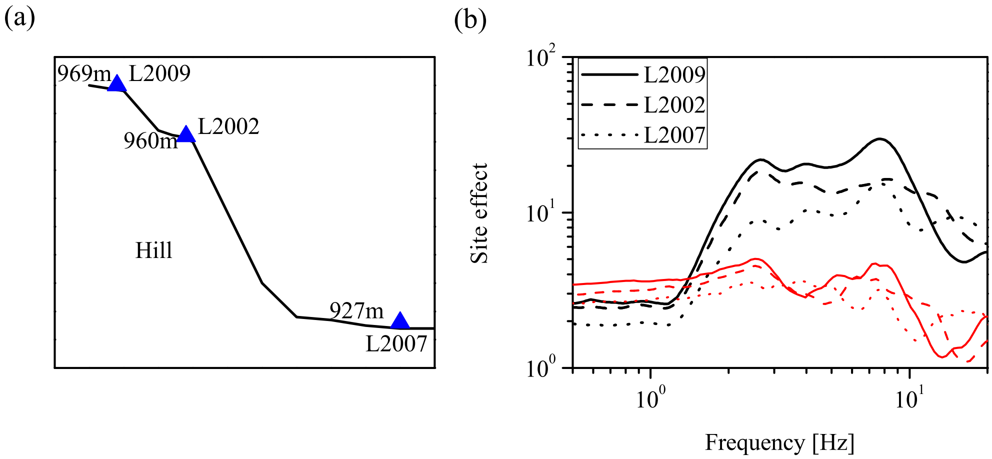

Figure 16. (a) Location illustration of the terrain effect array; (b) site response functions determined by the non-parametric GIT (black) and HVSR method (red).

increased elevation and is 1.5–2.0 times larger at L2009 than that at L2007. The site amplifications given by the HVSR method have no significant difference at the three stations, implying the HVSR method may not effectively reflect the local terrain effect. This result is in agreement with the conclusion from other studies (Parolai *et al.* 2004; Massa *et al.* 2013).

CONCLUSIONS

Nine hundred twenty-eight strong-motion recordings with hypocentre distances smaller than 150 km were used for separating the source spectra, path attenuation and site responses in the frequency domain using the two-step non-parametric GIT. These recordings were obtained at 43 permanent and temporary strong-motion stations during 132 earthquakes of M_s 3.2–6.5, which occurred on or near the fault plane of the 2008 Wenchuan earthquake from 2008 May 12 to 2013 December 31.

We assumed that the path attenuation equals 1.0 at the reference distance of 30 km. As a result, the cumulative attenuation within this distance is transferred to the inverted source spectra when the trade-off between the source effect and site response is solved using a reference site. The cumulative attenuation was supposed as a ratio of the inverted source spectrum over the theoretical source spectrum for an M_s 6.5 earthquake. Its theoretical source spectrum was determined using the Fourier amplitude spectral ratio method. Then the inverted source spectra of all 132 earthquakes were corrected by the cumulative attenuation to obtain the real source spectra, which show approximately close to ω^{-2} decay at high frequencies. Furthermore, a grid-searching method was used to determine the best-fit seismic moment and corner frequency. Moreover, the stress drop, source radius, *S*-wave energy and apparent stress were successively calculated. We investigated the scaling properties of these source parameters, and draw the following conclusions:

(1) Moment magnitude M_w has a linear deviation from the surface wave magnitude M_s measured by CENC. M_w is generally lower than M_s, and is in agreement with previous studies. M_0 is approximately proportional to the f_c^{-3}, and $M_0 f_c^3 = 2.87 \times 10^{15}\,\mathrm{N \cdot m \cdot s^{-3}}$. The average *S*-wave energy-to-moment ratio is close to 1.32×10^{-5}. The apparent stress σ_a is approximately equal to $0.74\Delta\sigma$, independent of the earthquake size.

(2) The value of stress drop $\Delta\sigma$ for individual earthquakes varies mainly from 0.1 to 1.0 MPa, following an approximately lognormal distribution with an average of 0.52 MPa. The value is significantly smaller than the median stress drop of interplate earthquakes (Allmann & Shearer 2009), and some other large earthquake sequences. It is also much smaller than the stress drop of the Wenchuan main shock which is similar to some other large earthquakes with similar magnitude ($\sim$8.0). This characteristic with low stress drop of Wenchuan aftershocks was investigated using the ε indicator. The results show that ε is less than 1.0, ranging from 0.75 to 0.85, indicating that the low stress drop may be interpreted by the partial stress drop mechanism. Explanations of the low stress drop in aftershocks may be related to the remaining locked parts on the fault plane of the main shock.

(3) The investigation shows that the stress drop $\Delta\sigma$ has no significant dependence on the earthquake size and the hypocentre depth, indicating that the Wenchuan aftershocks follow self-similarity over the M_w range of our data. The stress drop of aftershocks may be correlated to the slip distribution on the fault plane of the Wenchuan main shock. A relatively larger stress drop appeared at areas with relatively smaller slip.

The geometrical spreading is weak around the Wenchuan area within distances of $R = 30$–150 km, and is strongly dependent on the frequency. The *S*-wave quality factor $Q_s(f)$ is regressed by $Q_s(f) = 151.2f^{1.06}$. The quality factor shows strong dependence on frequency, which can be ascribed to the high heterogeneity of the crustal medium. Our study region is located on the southeast edge of the Tibet Plateau where the elevation suddenly drops from about 4500 m on the plateau to 500 m in the Sichuan Basin.

The inverted site responses of three stations from a terrain effect array show that the site amplification is strongest at the hilltop and smallest at the hillfoot, implying that the local topography considerably affects the ground motions. The site responses, calculated using the HVSR method, were not very different among the three stations. This suggests that the HVSR method may not be effectively used for analysing the local topography effect on ground motion.

ACKNOWLEDGEMENTS

This work is supported by the Science Foundation of Institute of Engineering Mechanics, China Earthquake Administration under grant no. 2016A04, Nonprofit Industry Research Project of China Earthquake Administration under grant no. 201508005 and National Natural Science Foundation of China under grant no. 51308515. We are grateful to the editor Dr Ana Ferreira, Sylvia Hales and two anonymous reviewers for their valuable comments that helped improve our work.

All the strong-motion recordings in this paper were derived from the China Strong Motion Network Center at www.csmnc.net, (last accessed 2015 December). Earthquake parameters, including hypocentre location and measured magnitude M_s, were obtained from China Earthquake Network Center at www.csndmc.ac.cn, (last accessed 2015 December). Moment magnitude M_w in the Global Centroid-Moment-Tensor catalogue was obtained from http://www.globalcmt.org/CMTsearch.html, (last accessed 2015 December). ρ_s, β_s and α_s were derived from the CRUST1.0 model at http://igppweb.ucsd.edu/~gabi/crust1.html.

REFERENCES

Abrahamson, N.A., Silva, W.J. & Kamai, R., 2014. Summary of the ASK14 ground-motion relation for active crustal regions, *Earthq. Spectra,* **30,** 1025–1055.

Allmann, B.P. & Shearer, P.M., 2009. Global variations of stress drop for moderate to large earthquakes, *J. geophys. Res.,* **114,** B01310, doi: 10.1029/2008JB005821.

Ameri, G., Oth, A., Pilz, M., Bindi, D., Parolai, S., Luzi, L., Mucciarelli, M. & Cultrera, G., 2011. Seperation of source and site effects by generalized inversion technique using the aftershock recordings of the 2009 L'Aquila earthquake, *Bull. Earthq. Eng.,* **9,** 717–739.

AQSIQ, 2015. GB18306—2015 Seismic Ground Motion Parameters Zonation Map of China, first edition, pp. 165-189, Standard Press of China, Beijing.

Atkinson, G.M. & Mereu, R.F., 1992. The shape of ground motion attenuation curves in southeastern Canada, *Bull. seism. Soc. Am.,* **82,** 2014–2031.

Babaie Mahani, A. & Atkinson, G.M., 2013. Regional differences in ground-motion amplitudes of small-to-moderate earthquakes across North America, *Bull. seism. Soc. Am.,* **103,** 2604–2620.

Bindi, D., Castro, R.R., Franceschina, G., Luzi, L. & Pacor, F., 2004. The 1997–1998 Umbria-Marche sequence (central Italy): source, path, and site effects estimated from strong motion data recorded in the epicentral area, *J. geophys. Res.,* **109,** B04312, doi: 10.1029/2003JB002857.

Bjerrum, L.W., Sørensen, M.B. & Atakan, K., 2010. Strong ground-motion simulation of the 12 May 2008 M_w 7.9 Wenchuan earthquake, using various slip models, *Bull. seism. Soc. Am.,* **100,** 2396–2424.

Boore, D.M., Stewart, J.P., Seyhan, E. & Atkinson, G.M., 2014. NGA_West2 equations for predicting PGA, PGV, and 5%-damped PSA for shallow crustal earthquakes, *Earthq. Spectra,* **30,** 1057–1086.

Bora, S.S., Scherbaum, F., Kuehn, N., Stafford, P. & Wdwards, B., 2015. Development of a response spectral ground-motion prediction equation (GMPE) for seismic-harzard analysis from empirical fourier spectral and duration models, *Bull. seism. Soc. Am.,* **105,** 2192–2218.

Brune, J.N., 1970. Tectonic stress and the spectra of seismic shear waves from earthquakes, *J. geophys. Res.,* **75,** 4997–5009.

Brune, J.N., Fletcher, J., Vemon, F., Haar, L., Hanks, T. & Berger, J., 1986. Low stress-drop earthquakes in the light of new data from Anzam California telemetered digital array, in *Earthquake Source Mechanics, Geophysical Monograph*, Vol. 37, pp. 237–245, America Geophysical Union.

Castro, R.R., Anderson, J.G. & Singh, S.K., 1990. Site response, attenuation and source spectra of S waves along the Guerrero, Mexica, subduction zone, *Bull. seism. Soc. Am.,* **80,** 1481–1503.

Castro, R.R., Pacor, F., Bindi, D. & Franceschina, G., 2004. Site response of strong motion stations in the Umbria, central Italy, region, *Bull. seism. Soc. Am.,* **94,** 576–590.

Chen, S.F., Wilson, C.J.L., Deng, Q.D., Zhao, X.L. & Luo, Z.L., 1994. Active faulting and block movement associated with large earthquakes in the Min Shan and Longmen Mountains, northeastern Tibetan Plateau, *J. geophys. Res.,* **99,** 24 025–24 038.

Chen, J.H., Liu, Q.Y., Li, S.C., Guo, B., Li, Y., Wang, J. & Qi, S.H., 2009. Seismotectonics study by relation of the Wenchuan Ms8.0 earthquake sequence, *Chin. J. Geophys.,* **52,** 390–397 (in Chinese).

Chen, Y.T., Yang, Z.X., Zhang, Y. & Liu, C., 2013. From 2008 Wenchuan earthquake to 2013 Lushan earthquake, *Sci. Sin. Terrae,* **43,** 1064–1072 (in Chinese).

Cheng, W.Z., Chen, X.Z. & Qiao, H.Z., 2006. Research on the radiated energy and apparent strain of the earthquakes in Sichuan province, *Prog. Geophys.,* **21,** 692–699 (in Chinese).

Drouet, S., Cotton, F. & Gueguen, P., 2010. Vs30, κ, regional attenuation and Mw from accelerograms: application to magnitude 3–5 French earthquakes, *Geophys. J. Int.,* **182,** 880–898.

Drouet, S., Bouin, M. & Cotton, F., 2011. New moment magnitude scale, evidence of stress drop magnitude scaling and stochastic ground motion model for the French West Indies, *Geophys. J. Int.,* **187,** 1625–1644.

Dutta, U., Biswas, N., Martirosyan, A., Papageorgious, A. & Kinoshita, S., 2003. Estimation of earthquake source parameters and site response in Anchorage, Alaska from strong-motion network data using generalized inversion method, *Phys. Earth planet. Inter.,* **137,** 13–29.

Fielding, E.J., Sladen, A., Li, Z., Avouac, J., Burgmann, R. & Ryder, I., 2013. Kinematic fault slip evolution source models of the 2008 M 7.9 Wenchuan earthquake in China from SAR interferometry, GPS, and teleseismic analysis and implications for Longmen Shan tectonics, *Geophys. J. Int.,* **194,** 1138–1166.

Iwate, T. & Irikura, K., 1988. Source parameters of the 1983 Japan sea earthquake sequence, *J. Phys. Earth,* **36,** 155–184.

Hanks, T.C. & Kanamori, H., 1979. A moment magnitude scale, *J. geophys. Res.,* **84,** 2348–2350.

Hassani, B., Zafarani, H., Farjoodi, J. & Ansari, A., 2011. Estimation of site amplification, attenuation and source spectra of S-waves in the East-Central Iran, *Soil Dyn. Earthq. Eng.,* **31,** 1397–1413.

Husid, P., 1967. *Gravity Effects on the Earthquake Response of Yielding Structures*. *Report of Earthquake Engineering Research Laboratory*. California Institute of Technology.

Hua, W., Chen, Z. L. & Zheng, S.H., 2009. A study on segmentation characteristics of aftershock source parameters of Wenchuan M 8.0 earthquake in 2008, *Chin. J. Geophys.,* **52,** 365–371 (in Chinese).

Hwang, R.D., 2012. Estimating the radiated seismic energy of the 2010 M_L 6.4Jiasian, Taiwan, earthquake using multiple-event analysis, *Terr. Atmos. Ocean. Sci.,* **23,** 459–465.

Kanamori, H., 1994. Mechanics of earthquakes, *Annu. Rev. Earth Planet. Sci.,* **22,** 207–237.

Konno, K. & Ohmachi, T., 1998. Ground-motion characteristics estimated from ratio between horizontal and vertical components of microtremor, *Bull. seism. Soc. Am.,* **88,** 228–241.

Laske, G., Masters, G., Ma, Z. & Pasyanos, M., 2013. Update on CRUST1.0: a 1-degree global model of Earth's crust, *Geophys. Res. Abst.,* **15,** Abstract EGU2013-2658, https://igppweb.ucsd.edu/∼gabi/crust1.html#visualization.

Lyu, J., Wang, X.S., Su, J.R., Pan, L.S., Li, Z., Yi, L.W., Zeng, X.F. & Deng, H., 2013. Hypocentral location and source mechanism of the Ms7.0 Lushan earthquake sequence, *Chin. J. Geophys.,* **56,** 1753–1763 (in Chinese).

Mandal, P. & Dutta, U., 2011. Estimation of earthquake source parameters in the Kachchh seismic zone, Gujarat, India, from strong-motion network data using a generalized inversion technique, *Bull. seism. Soc. Am.,* **101,** 1719–1731.

Massa, M, Barani, S & Lovati, S., 2013. Overview of topographic effects based on experimental observations: meaning, causes and possible interpretations, *Geophys. J. Int.,* **197,** 1537–1550.

Matsunami, K., Zhang, W.B., Irikura, K. & Xie, L.L., 2003. Estimation of seismic site response in the Tangshan area, China, using deep underground records, *Bull. seism. Soc. Am.,* **93,** 1065–1078.

McCann, M.W.J., 1979. Determining strong motion duration of earthquakes, *Bull. seism. Soc. Am.,* **69,** 1253–1265.

Orowan, E., 1960. Mechanism of seismic faulting in rock deformation: a symposium, *Geol. Soc. Am. Mem.,* **79,** 323–345.

Oth, A., Bindi, D., Parolai, S. & Wenzel, F., 2008. S-Wave attenuation characteristics beneath the Veranca region in Romania: new insights from the inversion of ground-motion spectra, *Bull. seism. Soc. Am.,* **98,** 2482–2497.

Oth, A., Parolai, S., Bindi, D. & Wenzel, F., 2009. Source spectra and site response from S waves of intermediate-depth Varanca, Romania, earthquake, *Bull. seism. Soc. Am.,* **99,** 235–254.

Oth, A., Bindi, D., Parolao, S. & Giacomo, D.D., 2010. Earthquake scaling characteristics and the scale-(in)dependence of seismic energy-to-moment ratio: insights from KiK-net data in Japan, *Geophys. Res. Lett.,* **37,** L19304, doi: 10.1029/2010GL044572.

Oth, A., Bindi, D., Parolai, S. & Giacomo, D.D., 2011. Spectral analysis of K-NET and KiK-net data in Japan, part II: on attenuation characteristics, source spectra, and site response of borehole and surface stations, *Bull. seism. Soc. Am.,* **101,** 667–687.

Oth, A & Kaiser, A.E., 2014. Stress release and source scaling of the 2010–2011 Canterbury, New Zealand earthquake sequence from spectral inversion of ground motion data, *Pure appl. Geophys.,* **171,** 2767–2782.

Pacor, F. *et al*., 2016. Spectral models for ground motion prediction in the L'Aquila region (central Italy): evidence for stress drop dependence on magnitude and depth, *Geophys. J. Int.,* **204,** 697–718.

Parolai, S., Bindi, D., Baumbach, M., Grosser, H., Milkereit, C., Karakisa, S. & Zunbul, S., 2004. Comparison of different site response estimation techniques using aftershocks of the 1999 Izmit earthquake, *Bull. seism. Soc. Am.,* **94,** 1096–1108.

Ren, Y.F., Wen, R.Z., Yamanaka, H. & Kashima, T., 2013. Site effects by generalized inversion technique using strong motion recordings of the 2008 Wenchuan earthquake, *Earth. Eng. Eng. Vib.,* **12,** 165–184.

Savage, J.C. & Wood, M.D., 1971. The relation between apparent stress and stress drop, *Bull. seism. Soc. Am.,* **61,** 1381–1388.

Sharma, M.L. & Wason, H.R., 1994. Occurrence of low stress drop earthquakes in the Garhwal Himalaya region, *Phys. Earth planet. Inter.,* **85,** 265–272.

Shaw, B.E., 2013. Earthquake surface slip-length data is fit by constant stress drop and is useful for seismic hazard analysis, *Bull. seism. Soc. Am.,* **103,** 876–893.

Shaw, B.E., Richards-Dinger, K. & Dieterich, J.H., 2015. Deterministic model of earthquake clustering shows reduced stress drops for nearby aftershocks. *Geophys. Res. Lett.,* **42,** 9231–9238.

Sivaram, K., Kumar, D., Teotia, S.S., Rai, S.S. & Prekasam, K.S., 2013. Source parameters and scaling relations for small earthquakes in Kumaon Himalaya, India, *J. Seismol.,* **17,** 579–592.

Tusa, G., Brancato, A., Gresta, S. & Malone, S.D., 2006. Source parameters of microearthquakes at Mount St Helens (USA), *Geophys. J. Int.,* **166,** 1193–1223.

Vassiliou, M.S. & Kanamori, H., 1982. The energy release in earthquakes, *Bull. seism. Soc. Am.,* **72,** 371–387.

Wen, R.Z., Ren, Y.F., Zhou, Z.H. & Li, X.J., 2014. Temporary strong-motion observation network for Wenchuan aftershocks and site classification, *Eng. Geol.,* **180,** 130–144.

Xu, X., Wen, X., Yu, G., Chen, G., Kilinger, Y., Hubbard, J. & Shaw, J., 2009. Coseismic reverse- and oblique-slip surface faulting generated by the 2008 Mw 7.9 Wenchuan earthquake, China, *Geology,* **37,** 515–518.

Xu, Y., Herrmann, R.B. & Koper, K.D., 2010a. Source parameters of regional small-to-moderate earthquakes in the Yunnan-Sichuan region of China, *Bull. seism. Soc. Am.,* **100,** 2518–2531.

Xu, Y., Herrmann, R.B., Wang, C. & Cai, S., 2010b. Preliminary high-frequency ground-motion scaling in Yunnan and southern Sichuan, China, *Bull. seism. Soc. Am.,* **100,** 2508–2517.

Yang, Z.X., Waldhauser, F., Chen, Y.T. & Richard, P.G., 2005. Double-difference relocation of earthquakes in central-western China, 1992–1999, *J. Seismol.,* **9,** 241–264.

Yu, T. & Li, X.J., 2012. Inversion of strong motion data from source parameters of Wenchuan aftershocks, attenuation function and average site effect, *Acta Seismol. Sin.,* **34,** 621–632 (in Chinese).

Zhang, H.Z., Diao, G.L., Zhao, M.C., Wang, Q.C., Zhang, X. & Huang, Y., 2008. Discussion on the relationship between different earthquake magnitude scales and the effect of seismic station sites on magnitude estimation, *Earthq. Res. China,* **22,** 24–30.

Zhao, C.P., Chen, Z.L., Hua, W., Wang, Q.C., Li, Z.X. & Zheng, S.H., 2011. Study on source parameters of small to moderate earthquakes in the main seismic active regions, China mainland, *Chin. J. Geophys.,* **54,** 1478–1489 (in Chinese).

Zheng, Y., Ma, H.S., Lyu, J., Ni, S.D., Li, Y.C. & Wei, S.J., 2009. Source mechanism of strong aftershocks (Ms≥5.6) of the 2008/05/12 Wenchuan earthquake and the implication for seismotectonics, *Sci. China Ser. D.,* **52,** 739–753.

Zuniga, F.R., 1993. Frictional overshoot and partial stress drop, which one?, *Bull. seism. Soc. Am.,* **83,** 936–944.